

CHALMERS



Numerical simulations of the plastic deformation of insulating joints

Master's Thesis in Solid Mechanics

JOHANNES GUNNARSSON

Department of Applied Mechanics
Division of Computational and Material Mechanics/CHARMEC
CHALMERS UNIVERSITY OF TECHNOLOGY
Göteborg, Sweden 2009
Master's Thesis 2009:15

Numerical simulations of the plastic deformation of insulating
joints

Master's Thesis in Solid Mechanics
JOHANNES GUNNARSSON

Department of Applied Mechanics
Division of Computational and Material Mechanics/CHARMEC
CHALMERS UNIVERSITY OF TECHNOLOGY

Göteborg, Sweden 2009

Numerical simulations of the plastic deformation of insulating joints
JOHANNES GUNNARSSON

©JOHANNES GUNNARSSON, 2009

Master's Thesis 2009:15
ISSN 1652-8557
Department of Applied Mechanics
Division of Computational and Material Mechanics/CHARMEC
Chalmers University of Technology
SE-412 96 Göteborg
Sweden
Telephone: + 46 (0)31-772 1000

Chalmers Reproservice
Göteborg, Sweden 2009

Numerical simulations of the plastic deformation of insulating joints
Master's Thesis in Solid Mechanics
JOHANNES GUNNARSSON
Department of Applied Mechanics
Division of Computational and Material Mechanics/CHARMEC
Chalmers University of Technology

Abstract

Numerical simulations were carried out to evaluate the performance of insulating joints in railway tracks. Although insulating joints are considered weak spots on the track due to the imposed rail discontinuity, they are nevertheless essential to monitor and control train traffic. All simulations presented were conducted using the commercial FE code Abaqus. Results were extracted, processed and plotted with the help of the programming languages Python and Matlab. No dynamic effects were included in the simulations.

This study consists of three major parts: The first part was to compare hyper-elastic Neo-hookean and linear elastic material models for the insulating layer in the joint. The simulations showed that there was no significant difference in stresses or displacements between the two models.

Investigating the effects of increasing the stiffness of the insulating material was performed in the second part. The investigation showed that increased stiffness decreases the plastic deformation in the steel. However when increasing the stiffness the interfacial shear stress increases. This will promote failure of the glue that ties insulation and rail together.

The effect of having an inclined insulating joint was analyzed. Four different inclination angles θ , were tested ranging from 0° (no inclination) to 60° . By increasing the angle the plastic deformation in the steel on both sides of the insulating layer increased under pure rolling conditions. Inclination did not seem to cause any significant changes in interfacial shear stresses.

Finally a comparison was made of the vertical displacement of the wheel center between the quasi-static ABAQUS simulations and approximations derived from Newtonian physics. These approximations indicate that the time that it takes for the wheel to travel over the gap is not sufficient to allow for the wheel displacements predicted by the quasi-static simulations when traveling on a speed exceeding roughly 85 km/h.

Keywords: Insulating rail joint, plastic deformation, ratchetting, low-cycle fatigue, inclined joint, hyper-elastic material

Contents

Abstract	I
Contents	III
1 Introduction	1
2 Numerical models and tools	2
2.1 Geometry and boundary conditions of the FE model	2
2.1.1 Mesh	5
2.1.2 Loads	7
2.1.3 Contact modeling	7
2.1.4 Steps in the numerical simulation	8
2.2 Material models	10
2.2.1 Linear elastic material	10
2.2.2 Hyper-elastic material	10
2.2.3 Plasticity model built-in to Abaqus	11
2.2.4 Custom model	11
2.3 Postprocessing	11
2.3.1 Comparison of hyper-elastic to linear elastic insulating material	11
2.3.2 State of strain in the rail steel	11
2.3.3 Deterioration of the insulating layer	12
2.3.4 Accuracy and consistency	12
2.4 Static vs. dynamic simulation	14
3 Results	14
3.1 Hyper-elastic vs. linear-elastic model in the insulating layer	15
3.2 Increased stiffness of the insulating layer	16
3.2.1 Shear stresses in the rail/insulation interface	17
3.2.2 Strain magnitudes in the rail steel	17
3.3 Laterally inclined joint	18
3.3.1 Strain magnitudes in the rail steel	19
3.4 Custom constitutive model for the rail steel	24
3.4.1 Influence of load magnitude	24
3.4.2 Traction vs. pure rolling	26
3.4.3 Variable Young's modulus of the insulating layer	28
3.4.4 Many rollovers–Stabilization	29
3.5 Limitations of using static analysis	30
4 Discussion	31
5 Acknowledgments	32
A Material parameters	32
A.1 Built in Abaqus constitutive model	32
A.2 Custom model	32

1 Introduction

The use of insulating joints is a rather easy and reliable way to monitor rail traffic. By a small voltage difference between the rails, a traveling train conducts current between the two rails see figure 1.1. By measuring this short circuiting it is possible to determine on which rail segment the train is located. The insulating joints are designed to insulate track sections. The insulating material is usually nylon (polyamid). The nylon layer does not provide load carrying capacity but is necessary to keep objects and dirt off the gap, especially conducting objects like metal shavings that can cause interference. Different designs of insulating joints are employed, for example supported and unsupported joints (depends on the position of the supporting sleepers) and inclined joints. Insulating joints are generally weak spots of the track structure and have rather short service life as compared to the rail itself.

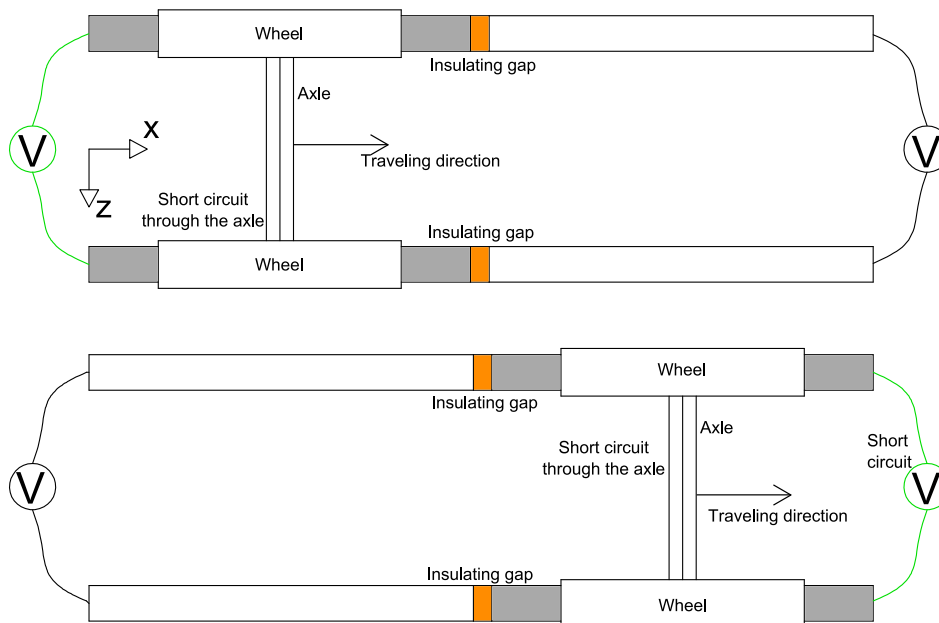


Figure 1.1: The role of insulating joints.

There is a high demand from the railway sector to increase the life span and reliability of these joints. To improve the performance it is first essential to understand why they fail. The biggest problem by using insulating gaps are the stress concentration on both ends of the rails caused by the imposed discontinuity. The insulating layer typically has a Young's modulus of 3-5 GPa as compared to the steel modulus of roughly 200 GPa.

The insulating joint is assembled with two fishplates on both sides of the ends of the rail web, an insulating layer and bolts to secure the connections, see figure 1.2. The gap between the two rail ends is on the order of 4 mm but varies between countries. The effects of the fishplate, bolts and support conditions will be ignored in this investigation. All simulations assume that the insulating joint is "supported" i.e. vertical deflections are restricted and the rail ends are not allowed to bend.



Figure 1.2: A photo of an assembled insulating joint.

2 Numerical models and tools

This chapter contains detailed information on how the Finite element model was designed, how simulations were performed and the subsequent postprocessing. The information can be helpful for future simulations of insulating joints. The investigation was conducted using the commercial software package Abaqus 6.7-2.

2.1 Geometry and boundary conditions of the FE model

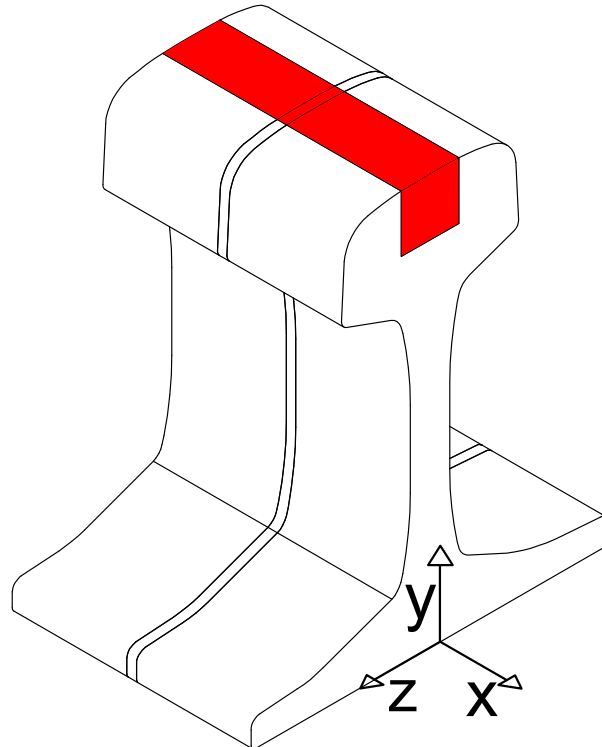


Figure 2.1: The simulated volume (red) in relation to the whole rail section.

The study considers a nominal UIC60 rail section which was imported to Abaqus from a CAD file of a 2D rail profile. To try to minimize the number of elements used in the

simulations and therefore reduce the calculation time only a small part of the rail was simulated as seen in figure 2.1. The width and height of the simulated volume was 24 mm X 24 mm. The length of the simulated volume varied between simulations. In all simulations except when simulating an inclined insulating gap (where the geometry is not symmetric) only half the volume was employed and symmetric boundary conditions were applied on the plane of symmetry seen in figure 2.2. The insulating gap was created by partitioning the rail volume thus making it possible to assign different material properties to different parts. In all simulations the gap size was $d_{\text{gap}} = 4$ mm.

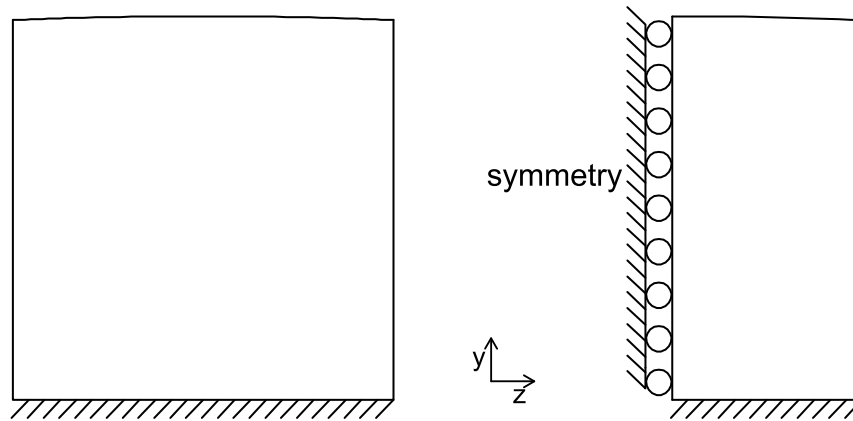


Figure 2.2: Boundary conditions of the rail part. On the left adopted boundary conditions for the case of an antisymmetric insulating joint, on the right boundary conditions for a symmetric joint.

When modeling the inclined joint the simulated rail volume was partitioned like in figure 2.3. θ represents the inclination of the joint from the z-axis of the global coordinate system, $\theta = 0^\circ$ equals a regular joint.

For all cases the boundary conditions at the bottom of the simulated volume were that all displacements were set to zero at all nodes of the bottom plane as seen in figure 2.2. Rotation of the model edge elements (in the x-direction) are prohibited. This corresponds to prohibited rail bending.

The wheel was modeled as an extruded circle with a radius $R_{\text{wheel}} = 460$ mm. An actual train wheel has "conic" shape as sketched in figure 2.4. This was not accounted for in the simulations where the wheel surface was considered cylindrical.

Rather than modeling the whole wheel, only a part was modeled to decrease computational efforts. A sketch of the modeled wheel can be seen in figure 2.5. A rigid link is defined between the theoretical center of the wheel and the upper surface of the wheel part as shown in figure 2.5

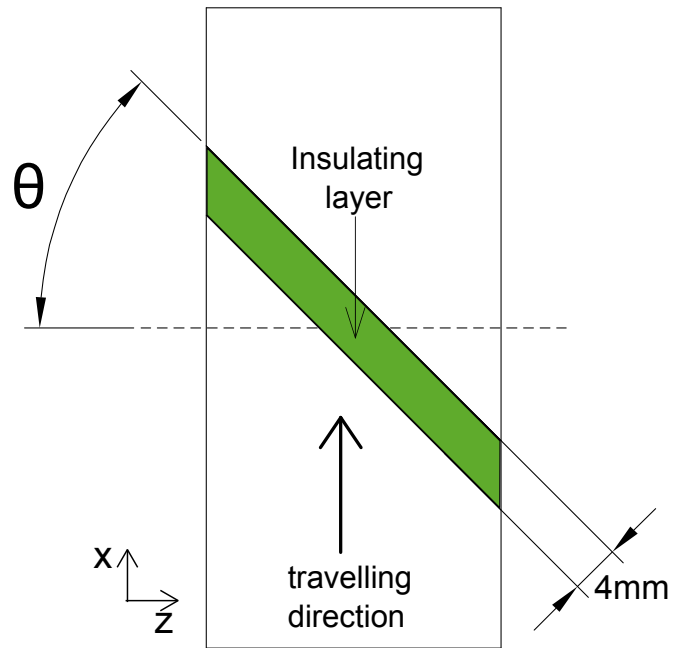


Figure 2.3: Inclined joint-Top view.

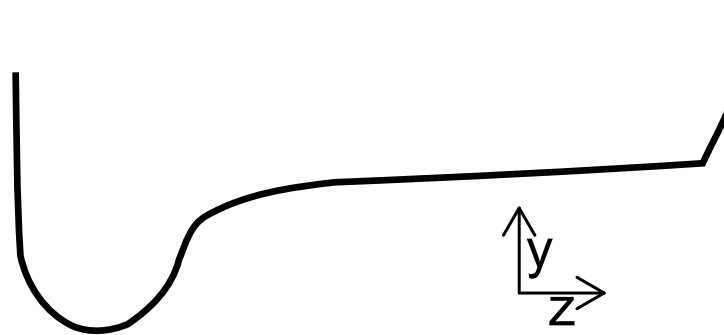


Figure 2.4: Surface profile of a real train wheel.

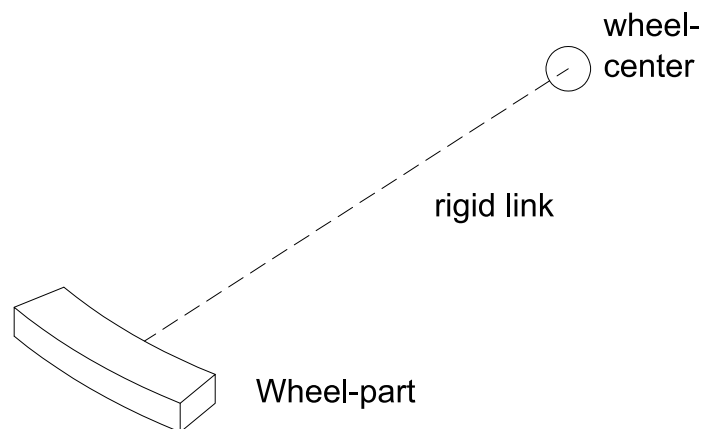


Figure 2.5: Modeling of wheel section

2.1.1 Mesh

The volume is meshed using two different shaped elements, tetrahedral and hexagonal as seen in figure 2.6. The hexagonal mesh is used on the region of interest i.e. the insulating gap and the steel surrounding it. It is necessary to have high resolution in this region to capture the high stress concentrations. The volume of the rail that was more than 5 mm away from the gap was meshed with tetrahedral elements and the mesh density was courser. Results from the course mesh were not used in the postprocessing. It was necessary to lower the wheel to the surface and also lift it up far away from the gap to get a good simulation of the rollover where the effects of lowering and lifting would not affect the results on the region of interest.

Three different mesh sizes were applied to the volume of interest i.e. the insulating layer itself and the rail steel on both sides. The mesh seed sizes were $a = 0.4, 0.5$ and 0.6 mm for different simulations. Two different types of elements were used on the area of interest for two different material models for the steel, these were hexagonal linear element with 1 and 8 integration points. Other elements on the rail are tetrahedral single integration point elements. To connect the two different shaped elements a "tie" constraint was defined between the surfaces of tetrahedral and hexagonal cells. Tie constraints tie two surfaces together so there is no relative displacement between them.

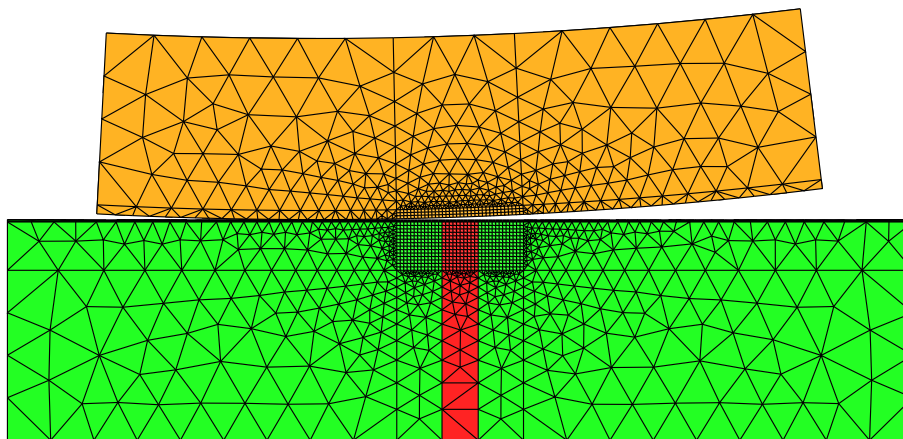


Figure 2.6: Meshed model for a symmetric joint.

Also the wheel was partitioned into two volumes with different types of elements so it would have the same element size and type as the matching point on the rail as seen in figure 2.7.

The elements on the boundary on the interface between the steel and insulating layer share nodes as seen in figure 2.8. In a real insulating joint the plastic is glued to the steel. However assuming that the glue layer is very thin as compared to the element size and also assuming that the glue is intact and have mechanical properties similar to that of the insulating layer this way of modeling the interface is reasonable.

When modeling the inclined joint a separate model was made for each joint inclination, due to the complexity of the model it was not possible to automate the modeling process by scripting. The meshed model of an inclined joint can be seen in figure 2.9. The wheel had to be meshed in the same way as the rail i.e. have a fine mesh on its surface to match the fine mesh on the rail in the vicinity of the insulating layer.

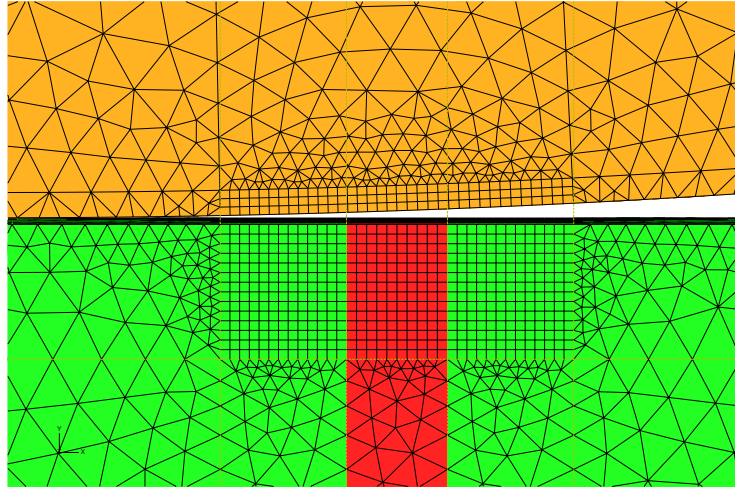


Figure 2.7: Meshed model-close up. Surface mesh of the wheel matches the mesh on the track surface.

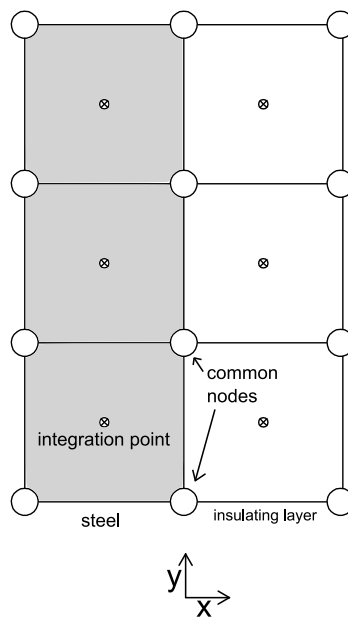


Figure 2.8: Interface between insulation and steel. The elements on the figure contain 1 integration point, in some simulations the elements contained 8 integration points.

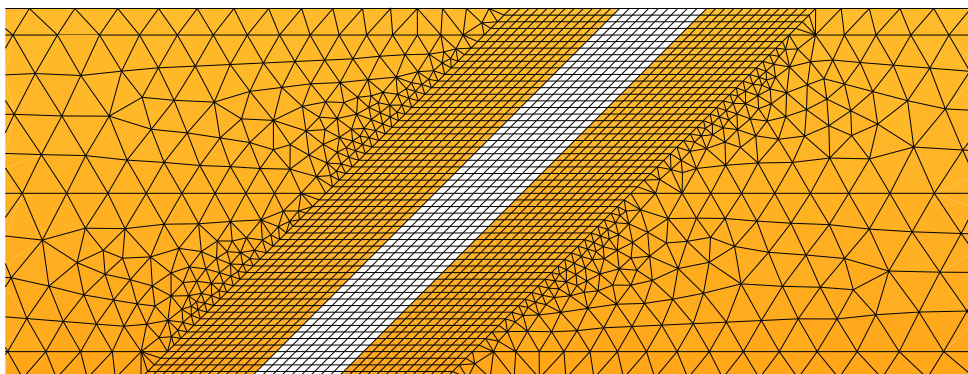


Figure 2.9: Top view of meshed inclined joint. The different colors represent different material, i.e. steel and nylon.

2.1.2 Loads

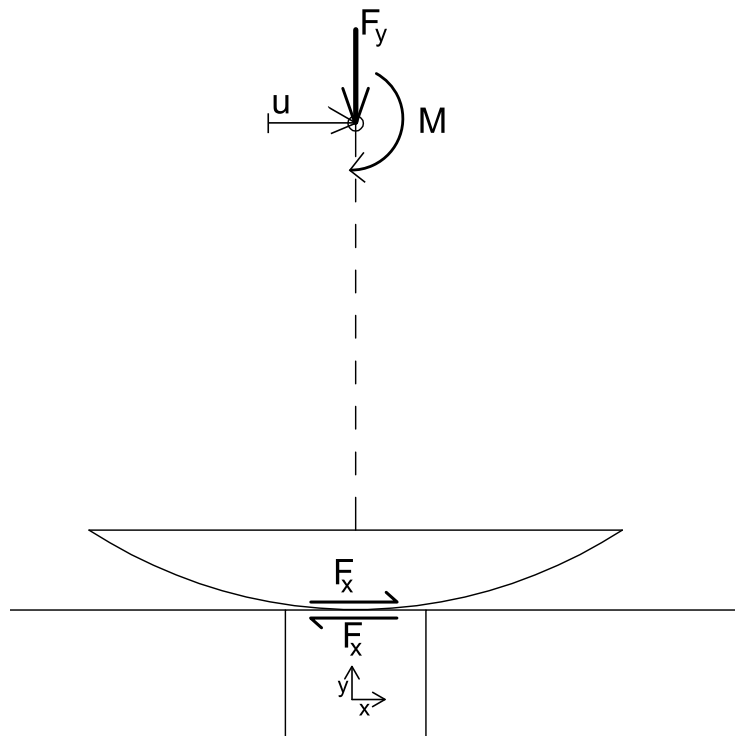


Figure 2.10: Loads, displacements and the resulting frictional force F_x .

All the loads and displacements were applied to a point corresponding to the center of the wheel. During each rollover three quantities define the loading: the horizontal displacement u of the wheel center in the traveling direction, the rotational moment M due to the traction and vertical load F_y due to the weight of the train. These are indicated in figure 2.10. The applied moment is calculated as

$$M = F_y R f \quad (2.1)$$

where R is the wheel radius and f is the traction coefficient defined as $f = F_x / F_y$ where F_x is the prescribed longitudinal force acting in the wheel/rail interface as seen in figure 2.10. In this study the traction coefficient is either $f = 0$ i.e. no traction or $f = 0.2$. Note that F_x is the result of the applied moment M . Transverse loads F_z are not considered in this study.

2.1.3 Contact modeling

The contact model used to simulate normal contact between the rail and the wheel is the built-in Abaqus Penalty(Standard) with linear contact stiffness. Tangential contact forces are evaluated using the Penalty module. The maximum coefficient of friction for the Coulomb friction used is $\mu = 0.4$. To ensure the wheel does not slide when rolling over the insulating gap when traction is applied on the wheel center it is necessary to define a maximum distance of allowed slip. The default value of "fraction of characteristic surface dimension" (FOCSD) was reduced from a value of 0.005 to 0.0025. FOCSD defines the maximum relative displacement between surfaces. When the wheel is directly above the center of the insulating layer as in figure 2.12, the risk of slipping is at maximum. The

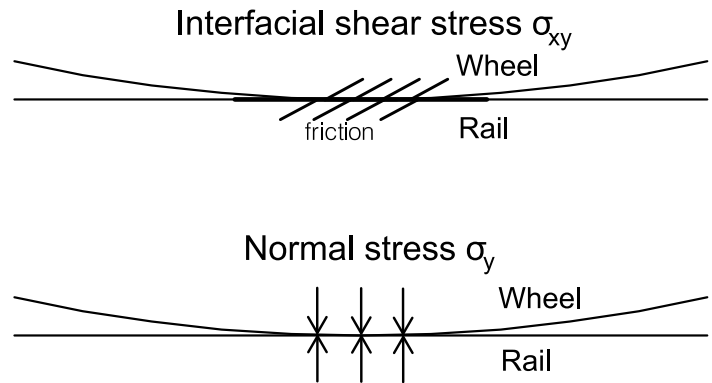


Figure 2.11: Normal and tangential stresses in the wheel/rail interface.

insulating layer is so flexible as compared to the steel that the wheel sinks into it and tangential force between the surfaces F_x decreases. In these quasi-static simulations wheel sliding can not be accounted for. In a simulation accounting for dynamics the wheel would gain a velocity v and the momentum of the train would ensure that the wheel would pass the gap without problem. In the present study reducing the value of the FOCSO ensured that the wheel did not slip.

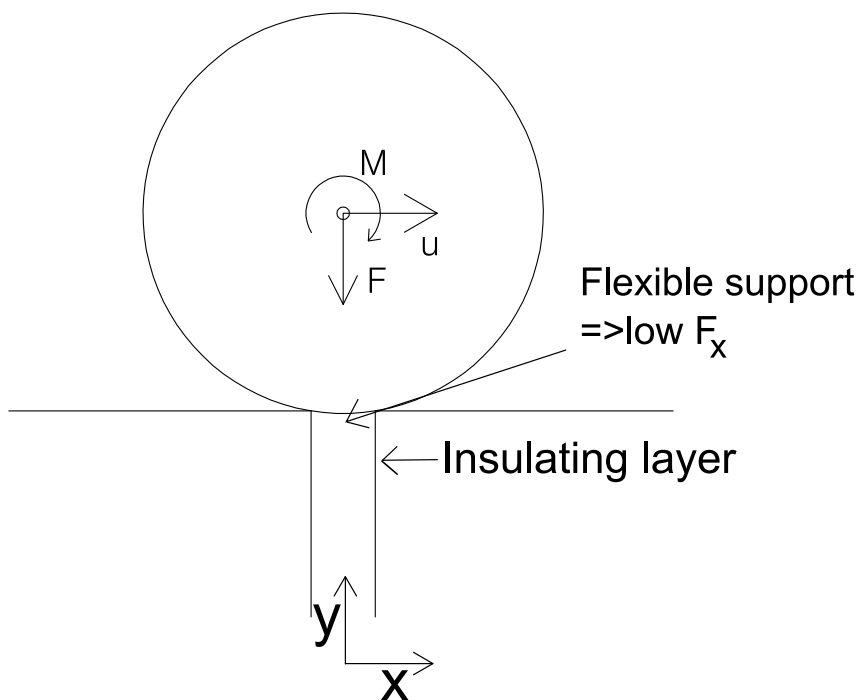


Figure 2.12: Risk of wheel slip in the static analysis when the wheel is positioned in middle of the insulating layer

2.1.4 Steps in the numerical simulation

When describing the load and the displacement it was necessary to use the theory of nonlinear geometry due to the great distance traveled by the wheel center during each rollover and also due to the large displacements of the element nodes. All simulations were

quasi-static i.e. acceleration and momentum is not accounted for. Further, the material models employed are (strain)-rate-independent.

A single rollover of the wheel consists of 8 steps as seen in figure 2.13 and described below.

- A** The first step consists in lowering the wheel on to the surface of the rail. To aid the normal contact model to converge, a point (anchor) above the center of the wheel was connected to the wheel center with a linear spring of stiffness $k = 5\text{kN/mm}$. Rather than solely prescribing the displacement of the wheel a much smoother contact is obtained by instead prescribing the movement of the anchor when lowering the wheel. It will further aid the establishment of the contact after the first rollover when the surface of the rail has yielded and it is not possible to know in advance how far the wheel should be lowered to obtain contact. All degrees of freedom of the wheel center are locked except u_y
- B** The vertical wheel load F_y is applied. In this step all degrees of freedom of the wheel center are locked except u_y , just like in the previous step.
- C** When the moment is applied, rotation of the wheel center around the z -axis ω_z is unlocked and the prescribed moment M is applied. When there is no interfacial shear considered, i.e. $f = 0$, then $M = 0$.
- D** For the rollover itself u_x on the wheel center is prescribed. The rotation angle ω_z is not prescribed during the rollover and the wheel rotates due to the interfacial wheel-rail friction.
- E** When the wheel has concluded the rollover, both the moment M and the vertical force F_y are set to zero.
- F1** Before starting the next rollover the wheel must be moved back to the initial position. The contact model is quite sensitive to large displacements so in this step u_x and ω_z are fixed and the wheel is lifted 1 mm up from the surface to release the contact.
- F2** The wheel is lifted up high above the rail before being moved back to the initial position in order for the contact algorithm not to make any attempts at contact iterations
- G** The wheel is moved to the initial position in front of the insulating layer and the next cycle can begin.

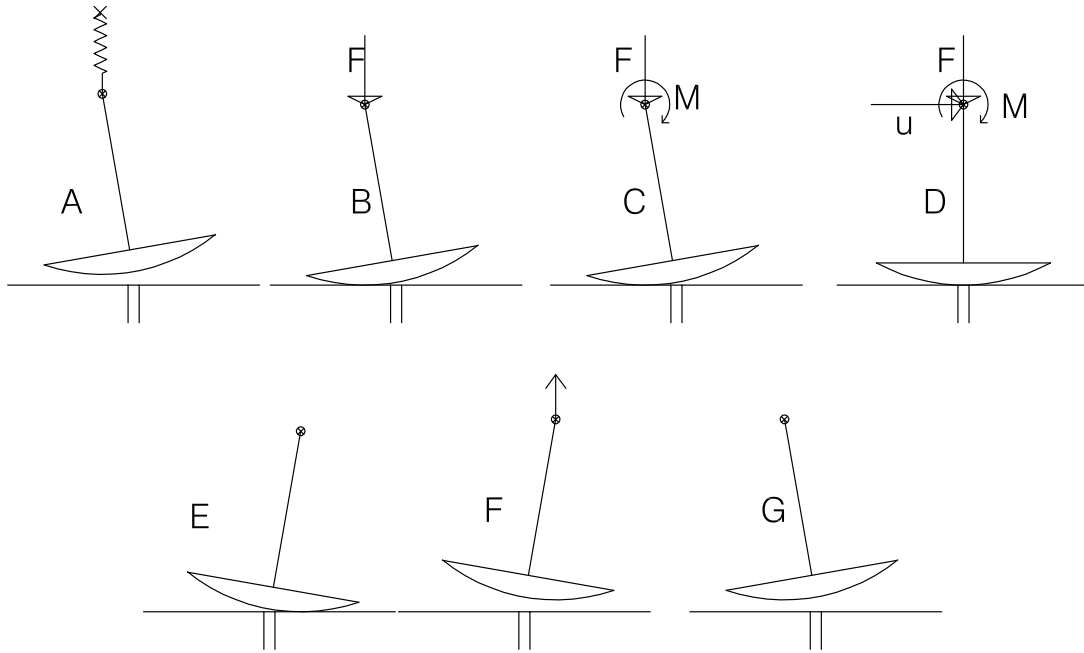


Figure 2.13: Steps for the 1 rollover in the simulation.

The input simulation steps were generated by a Python script.

2.2 Material models

Four different materials models were used in the simulations.

2.2.1 Linear elastic material

The wheel material was simulated as linear elastic in all simulations. The wheel steel had a Young's modulus of $E_{\text{wheel}} = 200$ GPa and Poisson's ratio of $\nu_{\text{wheel}} = 0.3$. In most simulations the insulating layer was considered as linear elastic. The Young's modulus of the insulating layer was varied between different simulations.

2.2.2 Hyper-elastic material

In many cases it is not accurate to model the behavior of the material by a linear-elastic model. When modeling a nearly incompressible isotropic material it is usually better to use a hyper-elastic model, especially under large strain conditions. The hyper-elastic stress strain relationship is derived from a strain energy density function $\Psi(\mathbf{F})$ where \mathbf{F} is the deformation gradient tensor of the element. A hyper-elastic material will initially behave linearly but for high strain magnitudes the elastic modulus λ will decrease significantly due to the release of energy.

The insulating layer usually consists of nylon as mentioned above. In most applications a more realistic behavior would be obtained by simulating the material as hyper-elastic instead of linear-elastic. One could further wonder if the displacements in the insulating layer are so large that they can't be considered as linear anymore. To investigate this, a built-in Abaqus Neo-Hookean hyper-elastic model was used and compared to a linear-elastic model for the insulating layer.

The stored energy of compressible Neo-Hookean material is, see [3]

$$\Psi = \frac{\mu}{2}(J^2 - 3) - \mu \ln J + \frac{\mu}{2}(\ln J)^2 \quad (2.2)$$

Where μ and λ are the initial bulk and elastic moduli and J the volume ratio between the initial and current state of the object, which in term is a function of the deformation gradient \mathbf{F} . It is easy to compare this model to a linear elastic model since they both use the same input parameters, i.e. $\lambda = \frac{E\nu}{(1+\nu)(1-2\nu)}$ and $\mu = \frac{E}{3(1-2\nu)}$.

2.2.3 Plasticity model built-in to Abaqus

Abaqus has a built in plasticity model that features a non-linear kinematic hardening model and can therefore simulate ratcheting, i.e. accumulation of plastic strain. This standard model is formulated in a small strain setting. This model has a benefit over the Custom Model that will be discussed in next section in that it converges well due to the good control over the time increments in the solver. The employed material parameters are found in the appendix, and are calibrated for the rail steel R260 (UIC900A) in [6].

2.2.4 Custom model

An advanced constitutive model especially designed for rail materials was employed in some of the simulations. The model uses nonlinear kinematic hardening of combined Armstrong-Frederick and Burlet-Cailletaud types. These hardening models were originally derived assuming small strains which is not quite valid for the steel surrounding the joint in these simulations. However a generalization to large strains featuring a Neo-Hooke description is also included in the model and is employed in this study. Strain-rate dependency is not included in the constitutive model. This is not a problem since all simulations were quasi-static. The material parameters have been identified for a rail steel in using test data [5] and are given in the appendix.

2.3 Postprocessing

In this section the postprocessing process of this study is described.

2.3.1 Comparison of hyper-elastic to linear elastic insulating material

To compare the two different material models of the insulating layer, i.e. the hyper-elastic and linear-elastic material, the von Mises stress σ_v and the magnitude of displacement u in the insulating material were compared between simulations featuring the two models. Usually when analyzing insulating joints the results from steel are analyzed to determine wear, plastic deformation and etc.. However since we are now comparing a feature of the insulating layer, the most straightforward approach is to compare the results evaluated in this layer.

2.3.2 State of strain in the rail steel

The Abaqus plasticity model calculates, for each integration point, a quantity called "equivalent plastic strain" which is defined as:

$$\epsilon_p = \epsilon_p|_0 + \int_0^t \sqrt{\frac{2}{3} \dot{\epsilon}_p : \dot{\epsilon}_p} dt \quad (2.3)$$

Here $\epsilon_p|_0$ is the initial equivalent plastic strain (taken as 0 in this study) and $\dot{\epsilon}_p$ are the plastic strain rate components. Note that the material models are not strain-dependant so the time is here irrelevant, therefore the integration is in fact carried out over the rollover.

The custom model doesn't include this measure to determine the deterioration so we use instead a so called *effective strain* which is defined for excessive plasticity i.e. $E\Delta\epsilon_{\text{eff}} \gg \Delta\sigma_{\text{eff}}$, where

$$\epsilon_{\text{eff}} = \sqrt{2/3} \sqrt{(\epsilon_{xx} - \epsilon_{yy})^2 + (\epsilon_{yy} - \epsilon_{zz})^2 + 6(\epsilon_{xy}^2 + \epsilon_{yz}^2 + \epsilon_{zx}^2)} \quad (2.4)$$

and

$$\sigma_{\text{eff}} = \sqrt{(\sigma_{xx} - \sigma_{yy})^2 + (\sigma_{yy} - \sigma_{zz})^2 + (\sigma_{zz} - \sigma_{xx})^2 + 3(\sigma_{xy}^2 + \sigma_{yz}^2 + \sigma_{zx}^2)} \quad (2.5)$$

and E is the Young's modulus of the material.

There are many different ways to quantify strain. One measure, commonly used for large non-linear deformation, is the so called *logarithmic strain*. Taking a 1D rod for example, logarithmic strain is defined by adding all the strain increments together when the rod is continuously stretched from the original length L to final length l [4]

$$\epsilon_L = \int_L^l \frac{dl}{l} = \ln \frac{l}{L} \quad (2.6)$$

In the current study ϵ_{eff} according to equation (2.4) is calculated by using the logarithmic strains from the integration points of the elements.

2.3.3 Deterioration of the insulating layer

The insulating layer does not carry much load due to its flexibility and does not deform enough to reach the yield limit of most plastic materials. However the insulating layer is glued to the steel on both sides and it is interesting to see if the glue can sustain the interfacial shear stress due to the heavy load from the wheel. The yielding of the steel on both sides of the insulating layer also causes larger and larger displacements after each wheel traversal and consequently a higher shear stress after each rollover. The glue that holds the two materials together is not part of the simulation as mentioned above so the shear stress σ_{xy} (in the yz -plane) was extracted from the integration points of the insulating layer elements on the interfaces between the two materials.

2.3.4 Accuracy and consistency

Just capturing the highest values in the model of the evaluation variables i.e. ϵ_p , ϵ_{eff} and σ_{xy} will not give realistic results. The elements on the edge between the rail surface and the interface between the steel and the plastic are the elements that deform the most. The mentioned values will become the highest there but the results will be very mesh dependent due to the high stress gradients. In [7] a mesh sensitivity test for two different mesh sizes was conducted for similar insulating joints. The result was that 1.5 mm into the steel, as defined in figure 2.14, the magnitudes of the measured quantities agreed between the fine and course mesh. Based on that result the values of ϵ_p , ϵ_{eff} and σ_v were evaluated at this position on both sides of the insulating layer. The values were extracted from the elements in the symmetry plane of the rail i.e. the xy -plane. To obtain the values at the exact position it was necessary to interpolate between values in the integration points of the elements. For the reduced integration elements, the elements only contained 1 integration point in the middle so there were no points to interpolate between in the z -direction. Hence only 2D interpolation was adopted in this case and values were taken 0.2 mm from the symmetry plane in the z -direction i.e. half the length of the elements (0.4 mm). The full integration elements have 8 integration points so it was possible to interpolate in 3D and

the values were taken from the 1.5 mm position although the elements were larger (0.5 mm).

For the shear stress σ_{xy} the results from the elements at the top surface of the rail were ignored due to the heavy distortion. Here results are evaluated at a depth of 0.6 mm below the top of the rail head.

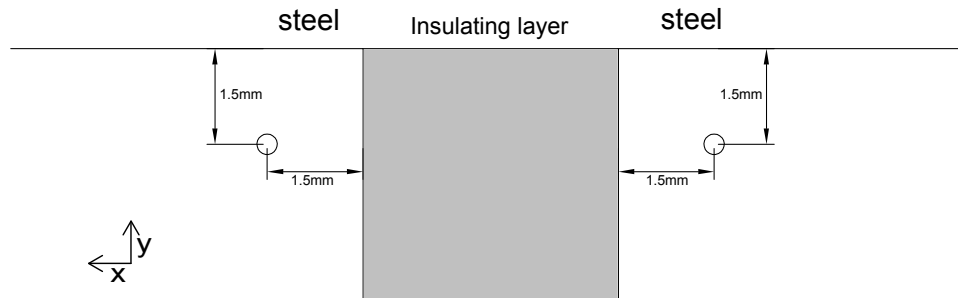


Figure 2.14: The position where values of ϵ_{eff} , ϵ_p and σ_v are evaluated.

When calculating ϵ_p for the inclined joint, the values were obtained from steel elements one element layer below the surface. The mesh size for these calculations was 0.6 mm, and each element contained one integration point so the values were evaluated at a distance 0.9 mm below the top of the rail head.

To calculate the maximum shear stress in the inclined insulating joint it was necessary to transform the stress matrices for each element from the global coordinate system to the orientation of the the plane between the steel and the insulating layer i.e. in the interface between the two materials. That was done by transforming the stresses using the tensor transformation rule

$$\boldsymbol{\sigma}' = \mathbf{R}_y \boldsymbol{\sigma} \mathbf{R}_y^T \quad (2.7)$$

where \mathbf{R}_y is the rotation matrix around the y-axis

$$\mathbf{R}_y(\alpha) = \begin{bmatrix} \cos(\alpha) & 0 & \sin(\alpha) \\ 0 & 1 & 0 \\ -\sin(\alpha) & 0 & \cos(\alpha) \end{bmatrix} \quad (2.8)$$

and $\alpha = -\theta$ where θ is the angle of inclination as defined in figures 2.3 and 2.15. $\boldsymbol{\sigma}$ is the 2nd order stress tensor defined as

$$\boldsymbol{\sigma} = \begin{bmatrix} \sigma_{xx} & \sigma_{xy} & \sigma_{xz} \\ \sigma_{yx} & \sigma_{yy} & \sigma_{yz} \\ \sigma_{zx} & \sigma_{zy} & \sigma_{zz} \end{bmatrix} \quad (2.9)$$

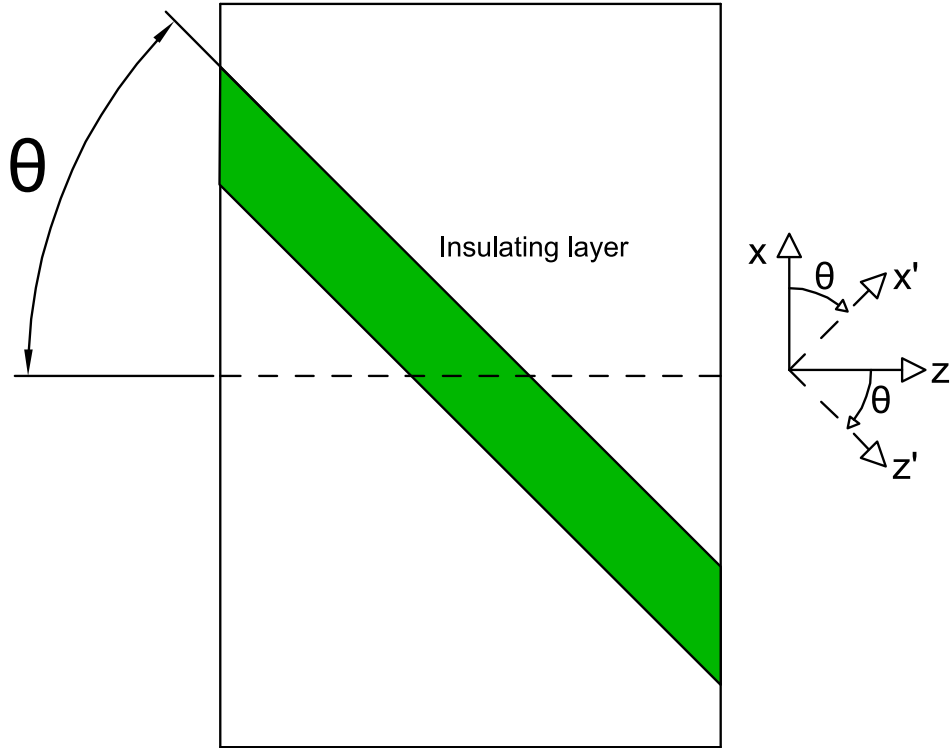


Figure 2.15: Stress transformation, the stress matrices for each element are rotated as seen in this figure to evaluate the stresses between the interface of the two materials.

2.4 Static vs. dynamic simulation

All simulations in this study were quasi-static and no dynamic effects are included. One could ask how good assumption it is to treat this as a static problem. When the wheel rolls over the gap the wheel sinks into the insulating layer and reaches a maximum vertical displacement when the wheel center is located directly above the middle of the insulating layer. To see if the wheel can drop this distance in the short time it takes it to travel over the joint a simplified evaluation (featuring Newton's second law) is employed. First to calculate the vertical position u_y of the wheel center we use

$$u_y = \frac{1}{2}a_y t^2 \quad (2.10)$$

where a_y is the vertical acceleration calculated as $a_y = F_y/m_{\text{wheel}}$, F_y is the spring force and m_{wheel} is the mass of the wheel. The vertical elongation of the spring is so small that that F_y is assumed as a constant. The time t is calculated as $t = u_x/v_{\text{train}}$ where v_{train} is the train velocity and u_x is the the horizontal displacement of the wheel center.

3 Results

In this section results are presented from all simulations. The simulations were carried out on a computer cluster. Each simulation was performed using four Xeon 5160 3 GHz processors with 4 GB of shared internal memory. The calculation time varied between 16 hours and 5 days depending on the number of elements in the model, distance traveled by the wheel center and which material model that was used for the rail steel.

3.1 Hyper-elastic vs. linear-elastic model in the insulating layer

The vertical force on the wheel was $F_y = 150$ kN with no rotational moment applied i.e. a traction coefficient of $f = 0$. These simulations were performed for different Young's moduli of the insulating layer E_{ins} , Poisson's ratio was kept constant $\nu_{\text{ins}} = 0.4$ for all cases. The mesh size for the insulating layer and surrounding steel is 0.4 mm. The elements of the insulating layer featured reduced integration i.e. they only contained one integration point.

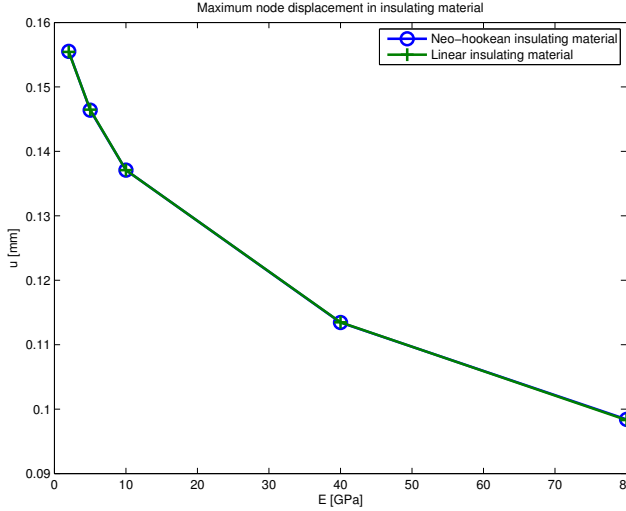


Figure 3.1: Maximum node displacement of the whole insulating layer during the last (forth) rollover of the wheel.

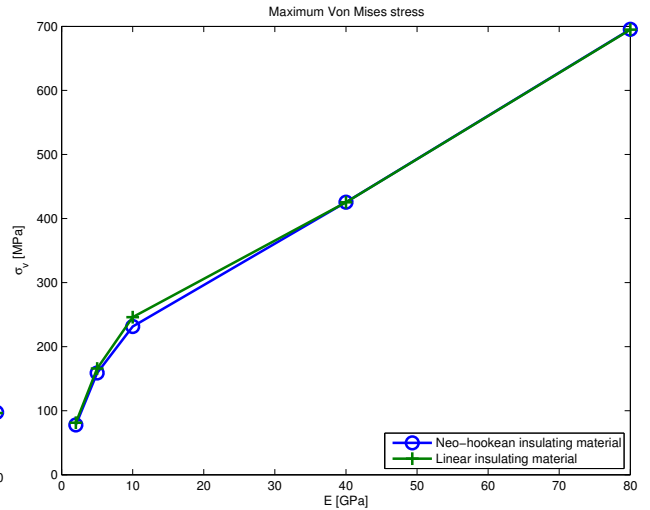


Figure 3.2: The maximum σ_v in the insulating layer during the last (forth) rollover of the wheel.

Figures 3.1 and 3.2 show the maximum displacement and maximum von-Mises stress in the insulating material during the last i.e. the 4th, rollover. The displacements are derived from element nodes and the von-Mises stresses from integration points. The maximum values of these two quantities from the whole insulating layer are plotted in figures 3.1 and 3.2. The results show that the difference between the two material models is small. The maximum displacements in figure 3.1 for different Young's modulus are almost identical. The von-Mises stress in figure 3.2 shows some difference in σ_v magnitudes for low values of the Young's modulus. Figure 3.3 to 3.6 show a more detailed evaluation for the extreme values of the Young's modulus i.e. $E_{\text{ins}} = 2$ GPa and $E_{\text{ins}} = 80$ GPa.

The peak displacement u are almost identical between the two material models for both $E_{\text{ins}} = 2$ GPa and $E_{\text{ins}} = 80$ GPa as seen in figures 3.3 and 3.4. However there is some difference in peak σ_v for $E_{\text{ins}} = 2$ GPa. The stress in the hyper-elastic material is lower as expected (see chapter 2.2.2). The reason for this small difference between the two material models is that the gap is so small as compared to the radius of the wheel that the deformation is not large enough to show the non-linear behavior of the hyper-elastic model. The largest displacements occur for the softest insulating layer i.e. $E_{\text{ins}} = 2$ GPa. This also corresponds to the largest plasticity in the steel that surrounds the insulating layer. This can be seen in figures 3.3 and 3.5 where the values of u and σ_v increase for each passage and the difference in σ_v between the two material models increases due to plastic deformation of the steel.

The conclusion from these simulations is that the difference in results between the material models i.e. the Neo-Hookean hyper-elastic and the linear elastic is small enough to be neglected. Using the hyper-elastic model could be more appropriate for larger gap sizes than the currently studied $d_{\text{gap}} = 4$ mm, where the displacement is larger and the

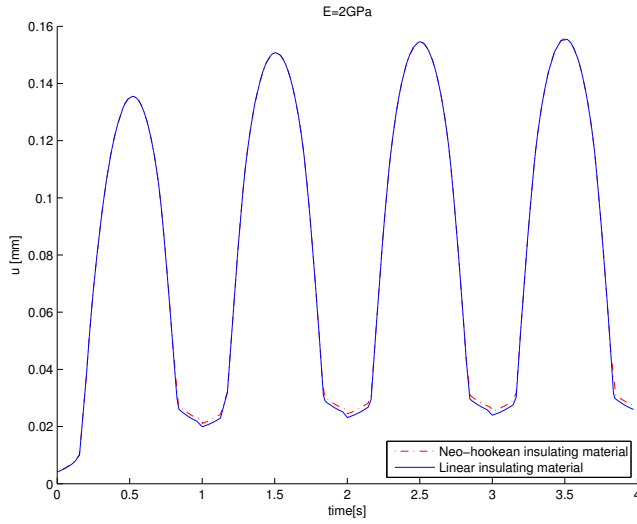


Figure 3.3: Displacement u for the 4 roll overs with $E_{ins} = 2$ GPa.

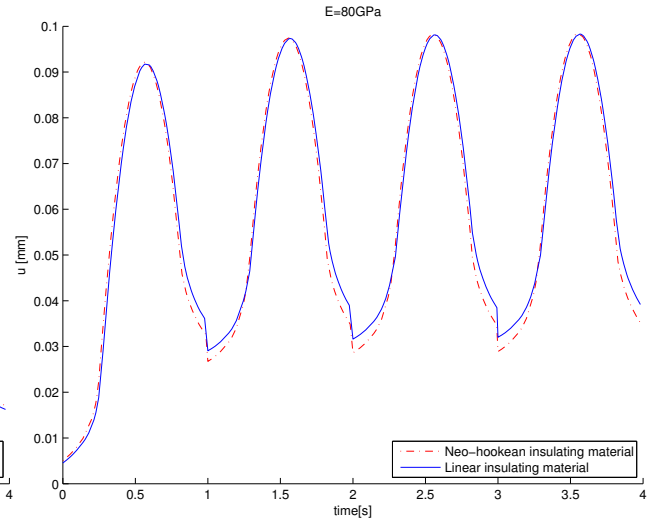


Figure 3.4: Displacement u for the 4 roll overs with $E_{ins} = 80$ GPa.

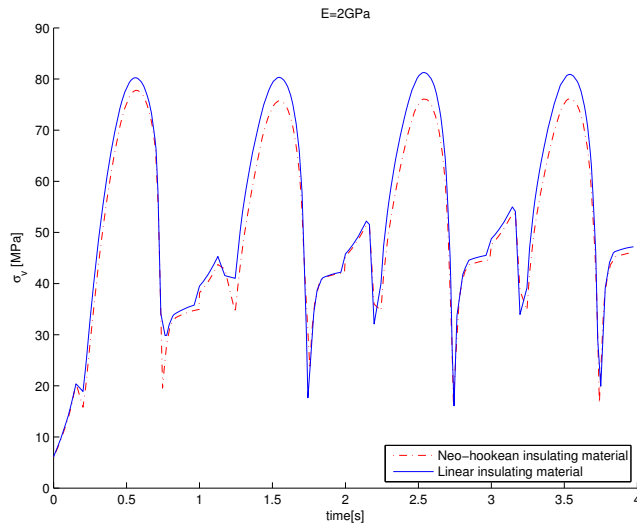


Figure 3.5: σ_v for all the 4 roll overs with $E_{ins} = 2$ GPa.

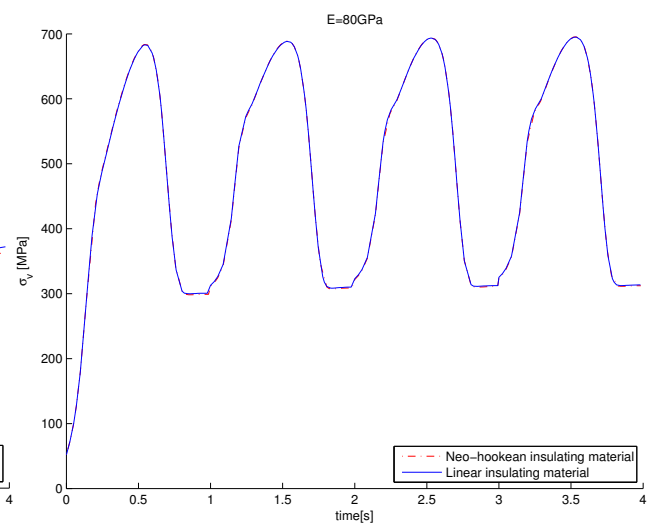


Figure 3.6: σ_v for all the 4 roll overs with $E_{ins} = 80$ GPa.

material behavior more non-linear. The calculation time for these two models differed only by 2% with the hyper-elastic model taking more time when simulating $E_{ins} = 2$ GPa. The reason for this small difference in calculation times is that the most time consuming parts of the simulation were the constitutive driver iterations for the steel material.

The simulations below were all performed using a linear elastic insulating layer.

3.2 Increased stiffness of the insulating layer

It is interesting to investigate if a stiffer insulating layer is beneficial for the joint. Both strains in the steel and shear stresses in the rail/insulation interface are evaluated below to answer this.

The vertical load was $F_y = 150$ kN and simulations included both cases of pure rolling $f = 0$ and tractive rolling $f = 0.2$. The mesh size was 0.4 mm and the elements contained one integration point. The built in Abaqus material model was employed for the rail steel. Material parameters are given in the appendix.

3.2.1 Shear stresses in the rail/insulation interface

In figures 3.7-3.8 the maximum shear stress in the outermost elements of the insulating layer at a depth of 0.6 mm below the rail head as described in chapter 2.3.4 are plotted. The shear stress from the elements at the surface were ignored due to the major distortion. The shear stresses are evaluated at the last (4th) rollover.

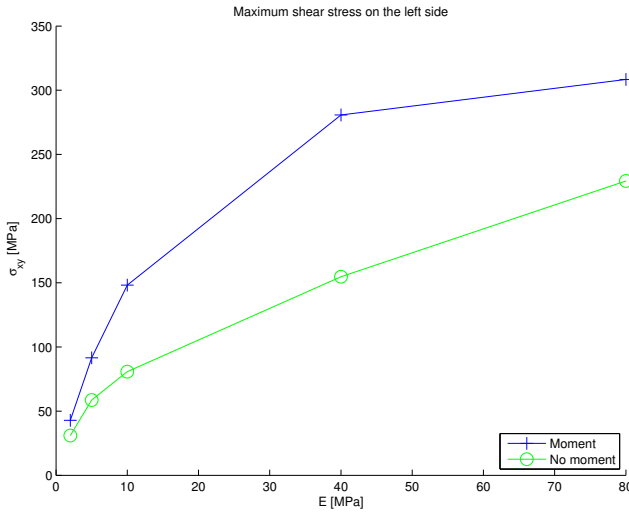


Figure 3.7: Maximum shear stress σ_{xy} on the left side ($x < 0$) of the joint.

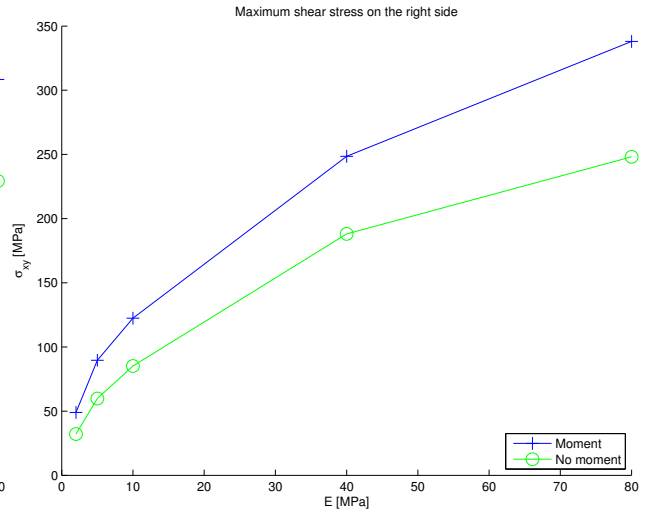


Figure 3.8: Maximum shear stress σ_{xy} on the right side ($x > 0$) of the joint.

The shear stress σ_{xy} increases rapidly with increased Young's modulus E_{ins} . By increasing E_{ins} from 2 GPa to 10 GPa it can be observed that on the left side the shear stress σ_{xy} increases by 160% for pure rolling and increases by 250% for tractive rolling. On the right side for the corresponding figures the values increase 160% and 150% respectively. The applied moment (traction) contributes more to σ_{xy} on the left than on the right hand side as seen in figures 3.7 and 3.8.

3.2.2 Strain magnitudes in the rail steel

The magnitudes of ϵ_p were extracted from the location defined in chapter 2.3.4. In figures 3.9 and 3.10 the results for pure rolling i.e. $f = 0$ are presented.

As seen in figures 3.9 and 3.10 a stiffer insulating layer (increasing the value of Young's modulus E_{ins}) decreases the plastic strains in the steel. This behavior is expected since an increased stiffness of the insulating layer results in an increased supporting capacity. The surrounding steel thus needs to take less load and the plastic deformation decreases. Note that ϵ_p is higher on the left side for all E_{ins} . Increasing Young's modulus from $E_{ins} = 2$ GPa to $E_{ins} = 10$ GPa decreases ϵ_p by 25% on the left hand side and by 15% on the right hand side after the 4th rollover. Having $E_{ins} > 10$ GPa is likely to be unrealistic for a plastic materials [1]. Materials that are both electricity insulating and very stiff e.g. ceramics are usually rather brittle and would not withstand the impact of the wheel. Note that in the current study the insulating material was only simulated as elastic i.e no yielding and hardening was considered, this is generally not a good approach when E_{ins} comes close to the stiffness of the rail steel ($E_{steel} = 200$ GPa).

Now consider the tractive rolling, with an applied moment calculated from equation (2.1) using $f = 0.2$. The behavior of ϵ_p is quite different as seen in figures 3.11 and 3.12. On the left hand side (figure 3.11). Plastic strain magnitudes ϵ_p are very similar, only a 3% difference between $E_{ins} = 2$ GPa and $E_{ins} = 10$ GPa. The lowest value of the ϵ_p magnitude

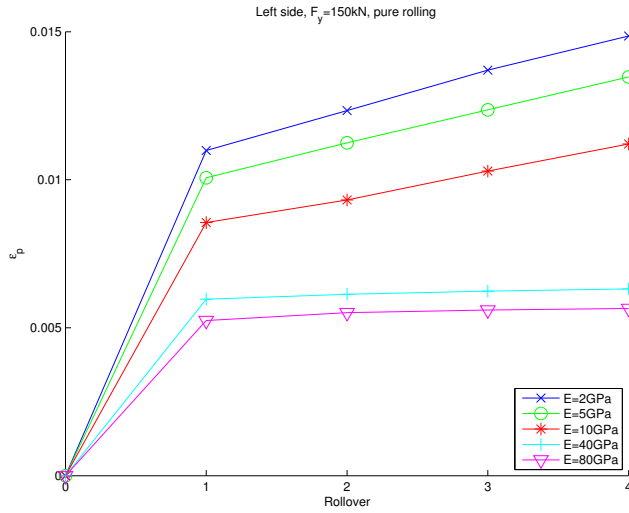


Figure 3.9: Equivalent plastic strain ϵ_p on the left hand side – Pure rolling.

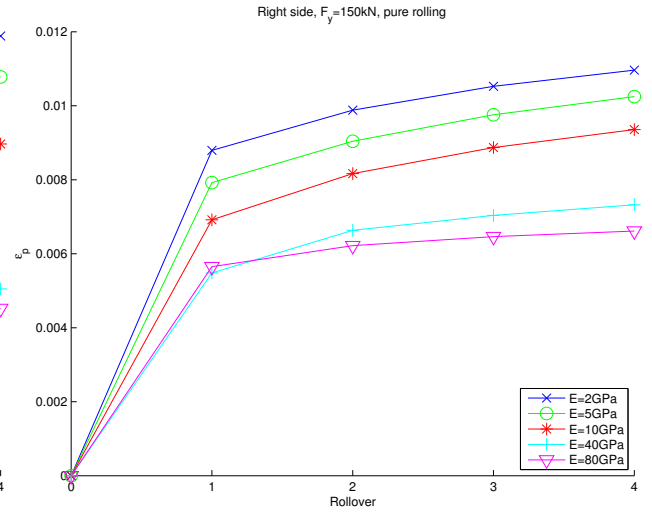


Figure 3.10: Equivalent plastic strain ϵ_p on the right hand side – Pure rolling.

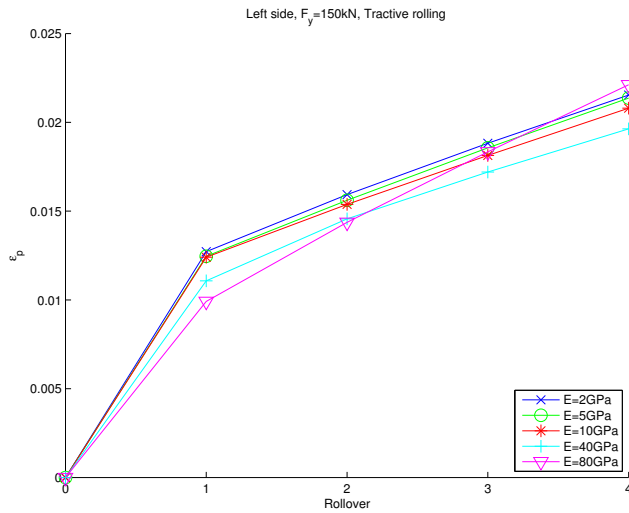


Figure 3.11: Plastic strain ϵ_p on the left hand side-Moment included $f = 0.2$.

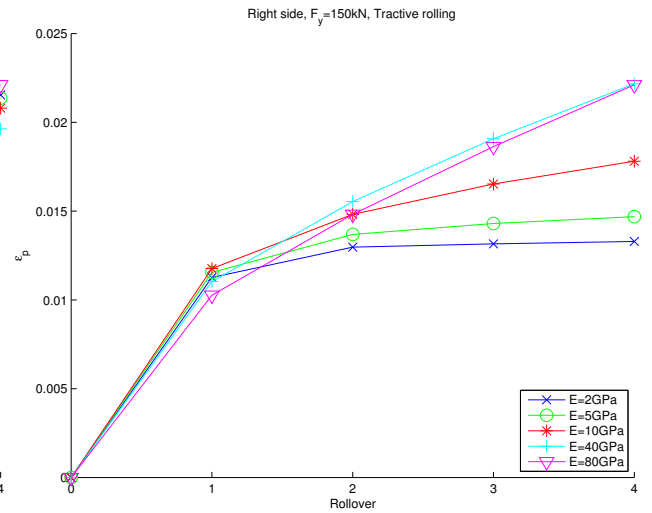


Figure 3.12: Plastic strain ϵ_p on the right hand side-Moment included $f = 0.2$.

after the 4th passage is obtained for $E_{\text{ins}} = 40$ GPa. Surprisingly the highest ϵ_p is obtained for $E_{\text{ins}} = 80$ GPa. The plastic strain at the right hand side of the rail is shown in figure 3.12. The quite surprising result is that an increased the stiffness of the insulating layer causes more yielding on the steel at the right hand side. This could be explained by the fact that the applied moment M introduces a compressive stress in the x -direction i.e. a high negative σ_{xx} . On the right hand side, the compressive stress σ_{xx} increases for higher E_{ins} due to increasing reaction force from the insulating layer. The result will be more yielding in the rail steel. This effect is explained better in chapter 3.4.2.

3.3 Laterally inclined joint

The insulating layer is in this part of the study considered to be nylon with $E_{\text{nylon}} = 3$ GPa and $\nu_{\text{nylon}} = 0.4$. The vertical load is $F_y = 150$ kN and the traction coefficient $f = 0$. The rail steel is simulated using the built-in Abaqus constitutive model with material properties given in the appendix. Four different angles are considered, 0° (not inclined), 30° , 45° and 60° . For all angles the mesh size is 0.6 mm for the dense mesh. The elements contain one

integration point. The simulations especially for the 60° angle took significantly more time to run than simulations of straight joints as the model has a large number of elements since symmetry can not be employed. Further the wheel had to travel a longer distance to roll over the joint. For this reason the mesh size was taken larger than in the other simulations.

3.3.1 Strain magnitudes in the rail steel

As mentioned in chapter 2.3.4 the ϵ_p magnitudes are evaluated at a depth of 0.9 mm from the top of the rail head in the elements that are closest to the insulating layer on both sides of the insulating gap. The maximum values of ϵ_p after each wheel passage are plotted in figures 3.13 and 3.14

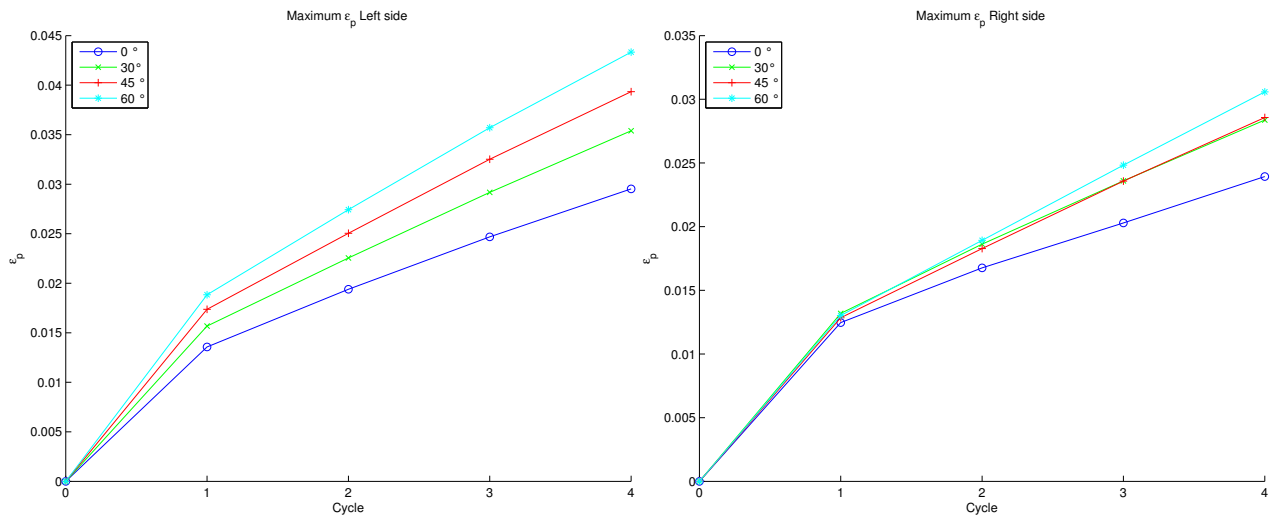


Figure 3.13: Maximum ϵ_p on the left hand side of the insulating joint. Figure 3.14: Maximum ϵ_p on the right hand side of the insulating joint.

As seen in figures 3.13 and 3.14 the equivalent plastic strain ϵ_p is lowest for 0° i.e. a straight joint and gradually increase both on the left and right hand side of the insulating layer for an increased angle of inclination θ . The curves for $\theta = 30^\circ$ and $\theta = 45^\circ$ are almost identical on the right hand side (wheel traveling from left to right).

In figures 3.15 and 3.16 the length of the affected region is indicated. The affected length is the distance in the projected z -direction (see figure 3.17) where elements have $\epsilon_p > 10^{-3}$ at the 4th rollover at a depth of 0.9 mm below the top of the rail head in the interface between the two materials as shown in figure 3.17.

As seen in figures 3.15 and 3.16 the affected projected length decreases for increasing angles on both sides. However if we consider the length of the affected zone as measured parallel to inclination the length will be increased by a factor $1/\cos(\theta)$ and the length of the zone will increase with an increasing inclination.

For a better understanding of the plastic strain as a function of z -position. Plotting is made for two different angles, $\theta = 0^\circ$ (not inclined) and $\theta = 60^\circ$ in figures 3.18-3.21

In 3.18 – 3.19 the ϵ_p magnitudes for a straight joint ($\theta = 0^\circ$) are plotted as a function of z -position. As seen ϵ_p increases after each roll over. The curves for both sides of the insulating layer are completely symmetric with maximum ϵ_p at the position $z = 0$ after each rolling which is expected since the geometry and loading are symmetric. Note that the values are higher on the left side than on the right side.

The corresponding plots for $\theta = 60^\circ$ are given in figures 3.20 and 3.21. The element coordinates are projected onto the z -axis as shown in figure 3.17. The curves have shifted

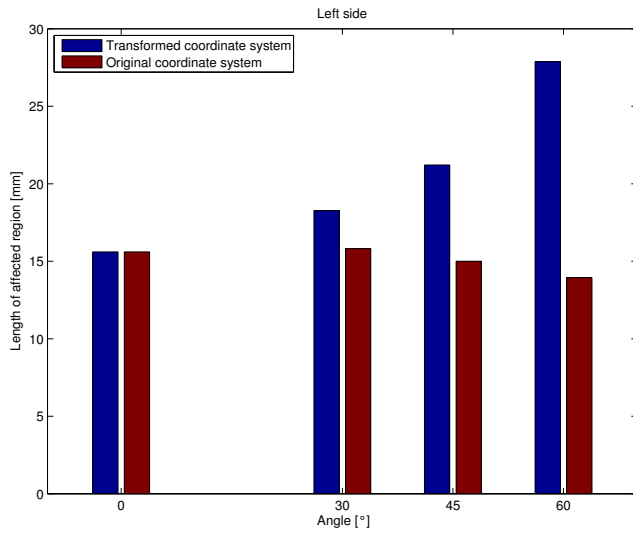


Figure 3.15: Length of the affected region on the left side. Projected on the z -axis

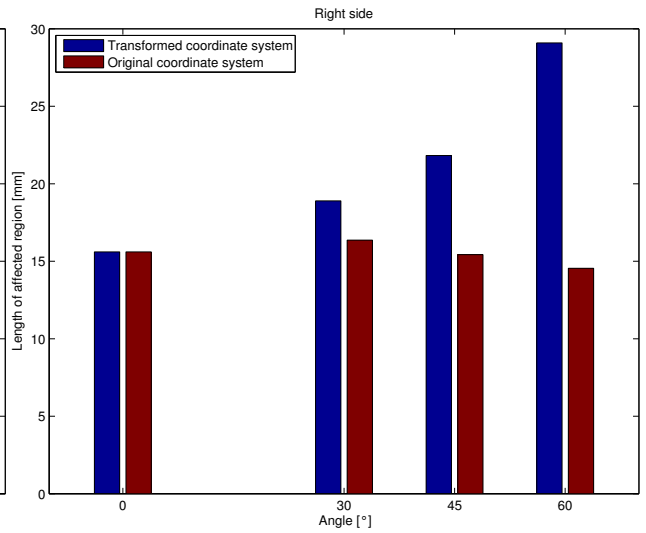


Figure 3.16: Length of the affected region on the right side. Projected on the z -axis

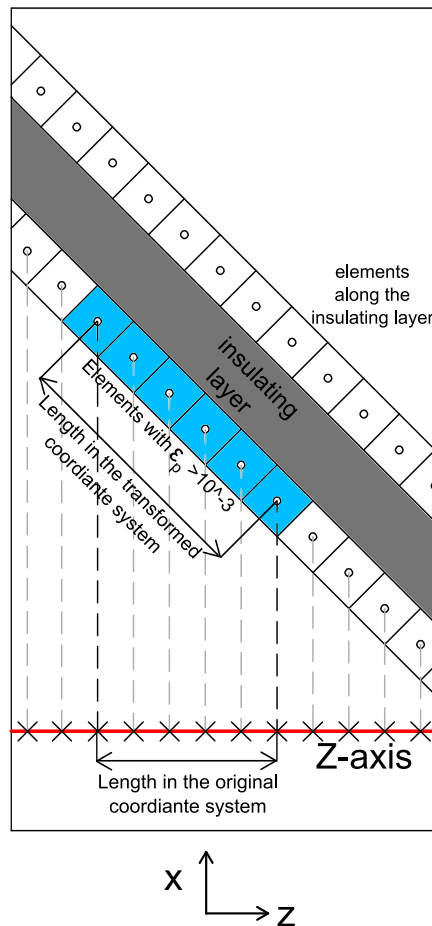


Figure 3.17: The ϵ_p magnitudes are evaluated at from elements closest to the insulating layer at depth of 0.9 mm from the surface. In figures 3.15, 3.16, 3.18 and 3.21 these values are projected on the z -axis like seen here

and are biased as compared to $\theta = 0^\circ$. On the left hand side of the insulating layer (wheel travels from left to right) the curves shift toward the negative z -direction. On the right

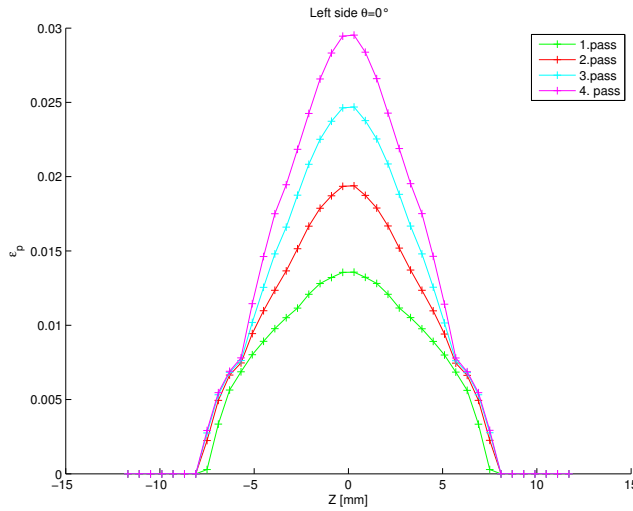


Figure 3.18: ϵ_p after each rollover for 0° angle joint on the left side of the insulating layer.

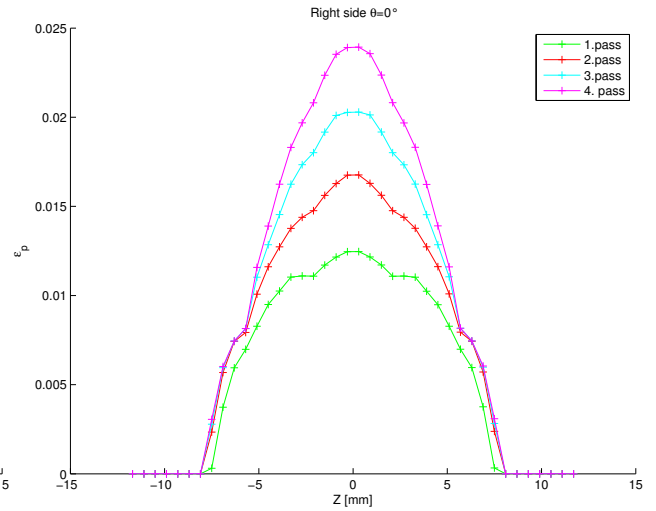


Figure 3.19: ϵ_p after each rollover for 0° angle joint on the right side of the insulating layer.

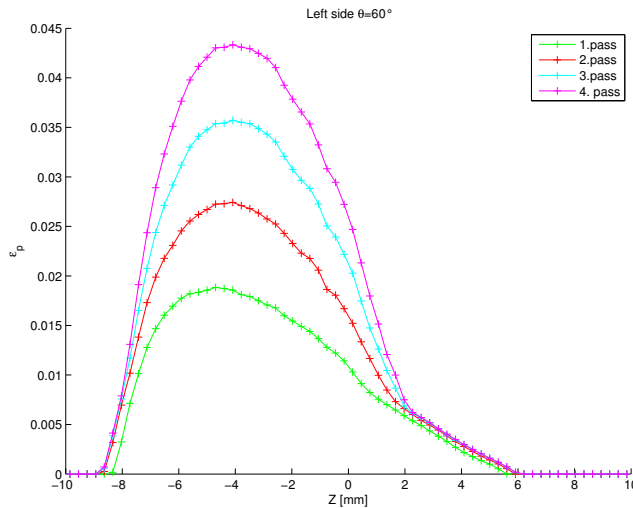


Figure 3.20: ϵ_p after each rollover for 60° joint on the left hand side of the insulating layer.

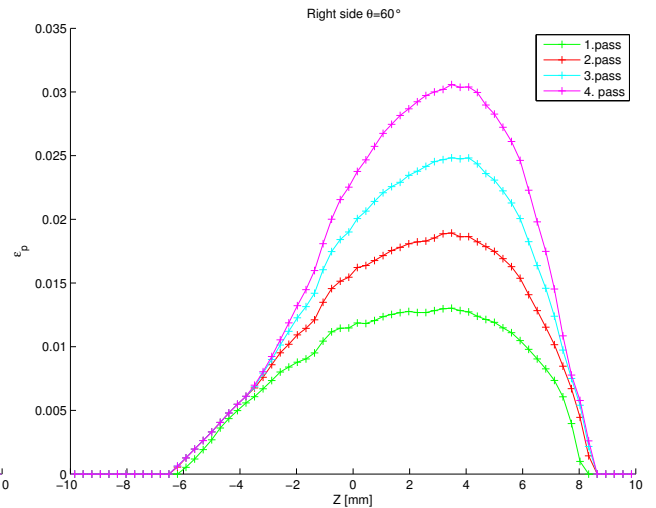


Figure 3.21: ϵ_p after each rollover for 60° joint on the right hand side of the insulating layer.

hand side of the insulating layer the curves shift towards the positive z -direction.

In figures 3.22 and 3.23 the maximum magnitudes of the shear stresses $\sigma_{x'y'}$ and $\sigma_{y'z'}$ in the insulating elements at the insulation/rail interface are shown. The results are from the 4th and final rollover. The stresses are projected from the original coordinate system as described in chapter 2.3.4 to get the shear stresses along the plane between the two materials. $\sigma_{x'y'}$ decreases significantly for increasing θ up to $\theta = 45^\circ$. The $\sigma_{y'z'}$ magnitude increases for increasing θ but decreases somewhat for $\theta = 60^\circ$. Note that the magnitudes of $\sigma_{x'y'}$ and $\sigma_{y'z'}$ for different θ are not from the same position or the same time step.

In figures 24(a)– 24(e) the wheel-rail contact pressure for the case of $\theta = 0^\circ$ during the first rollover is shown. The unit of the contact pressure is MPa.

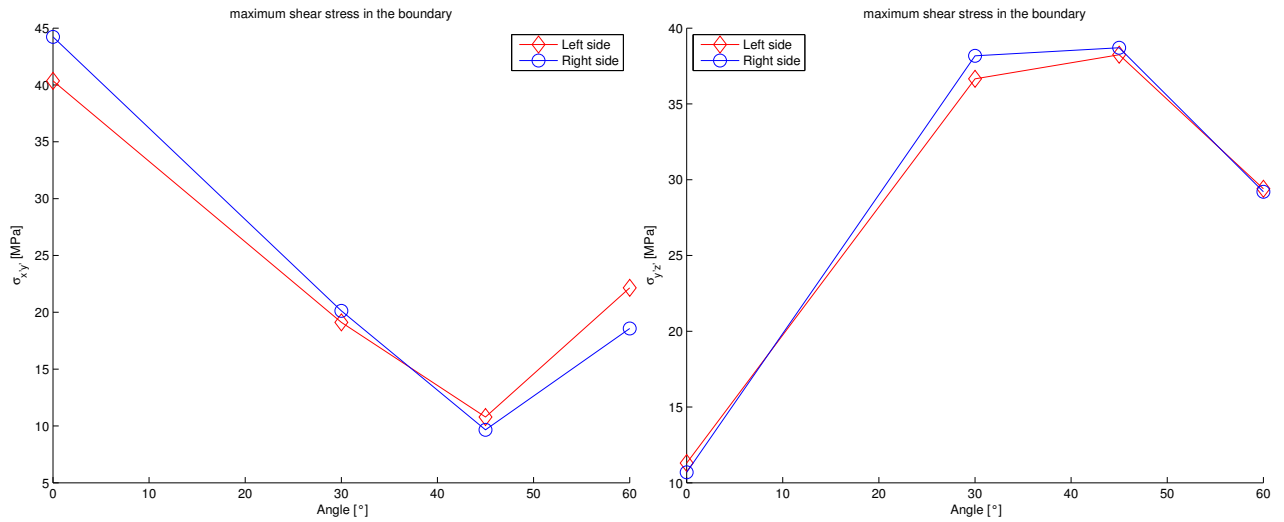


Figure 3.22: $\sigma_{x'y'}$ on the interface between the two materials.

Figure 3.23: $\sigma_{y'z'}$ on the interface between the two materials.

The contact patch is elliptical and symmetric around the x -axis for the whole rollover, though it is hard to see in the first and the last frame due to the course mesh. There is almost no contact pressure between the insulating layer and the wheel. The size of the contact patch increases when the wheel sinks into insulating layer as seen in figure 24(c) and causes extreme contact pressures on both sides of this layer.

In figures 25(a)– 25(e) the contact pressure is plotted for $\theta = 60^\circ$.

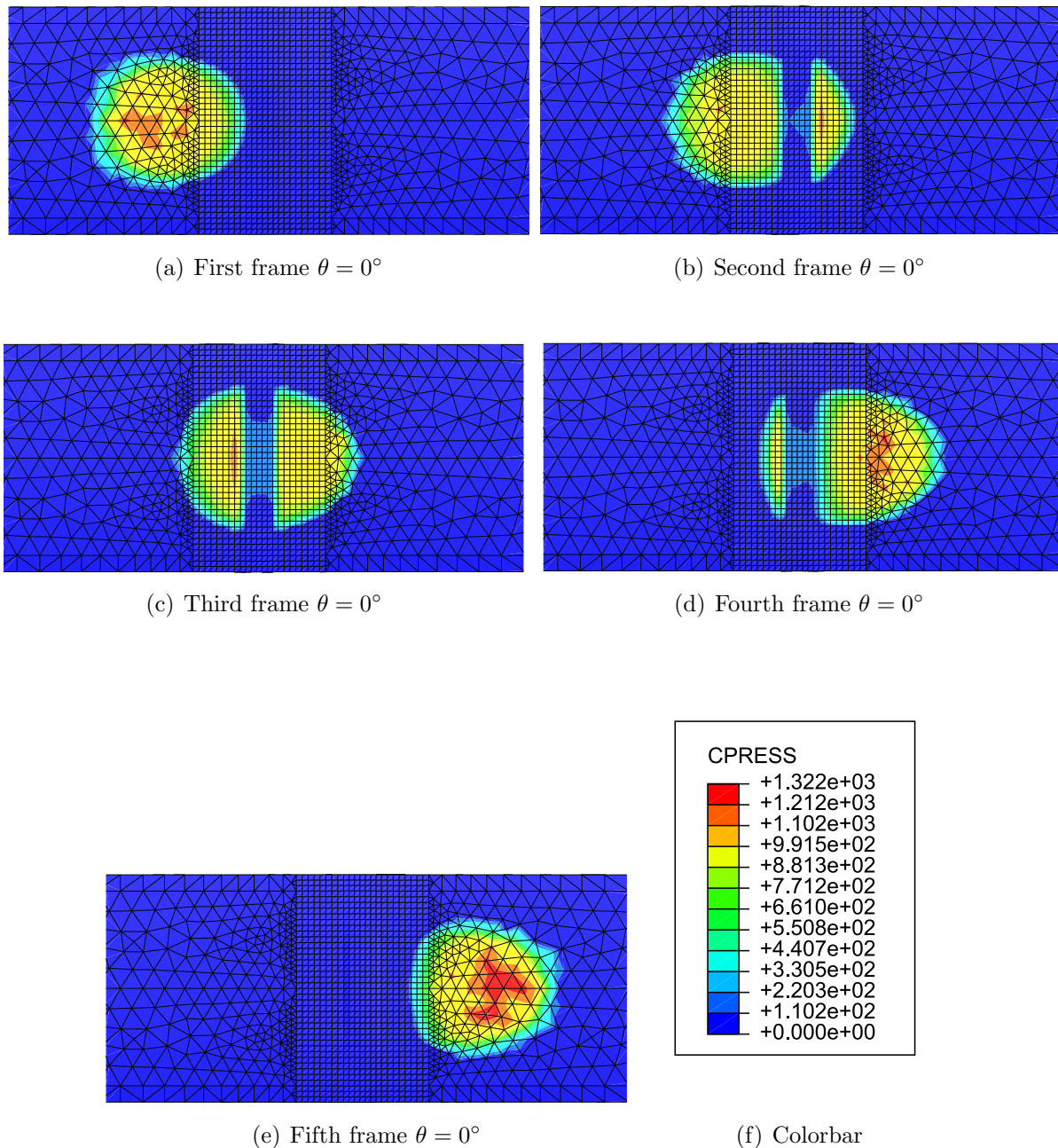


Figure 3.24: Contact pressure for $\theta = 0^\circ$

Here the contact patch is not symmetric. When the wheel is in the center of the gap as seen in figure 25(c), the contact patch has shifted on both sides of the gap. This explains the shifted maximum value of ϵ_p in figures 3.20 and 3.21. The contact patch shifts to the side of the steel away from the insulating layer since the insulating layer gives little support to the wheel. For increasing θ the influenced surface area of the insulating layer increases. This reduces the area of the contact region on the steel, which in turn increases the contact pressure. The increased contact pressure leads to higher stress magnitudes in the steel and therefore more yielding of the material

The results show that for the case considered an inclined joint is not beneficial for the steel, nor the for glue that connects the two materials. The steel yields more and the shear stresses on the interface of the two materials are about the same.

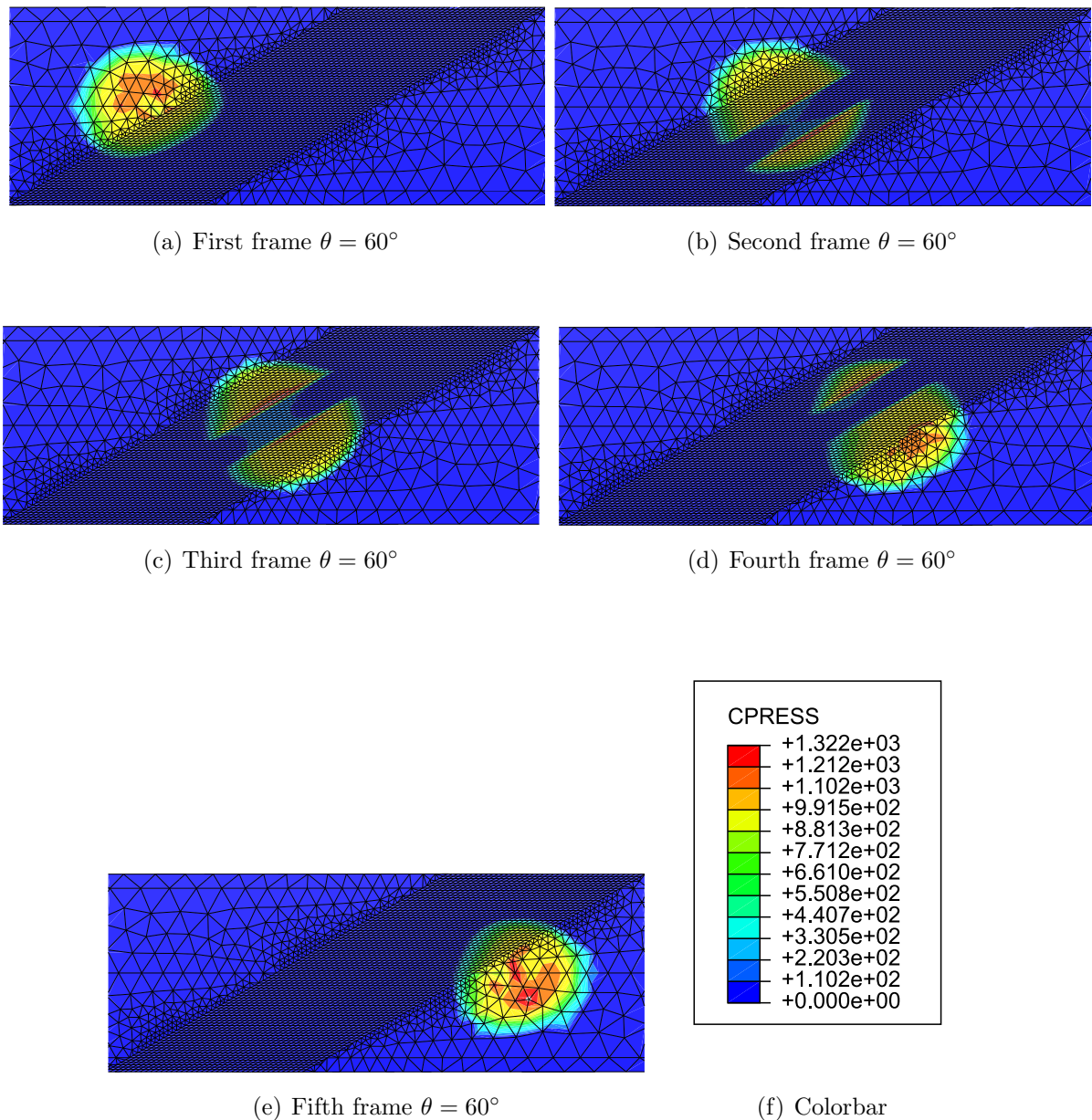


Figure 3.25: Contact pressure for $\theta = 60^\circ$

3.4 Custom constitutive model for the rail steel

The features of the constitutive model are discussed in chapter 2.2.4

A larger mesh size of 0.5 mm was used due to the computational demands of this material model. The elements in the region of interest contained 8 integration points.

3.4.1 Influence of load magnitude

Three different loads F_y were applied to the wheel, 100 kN, 150 kN and 200 kN, with and without applied moment i.e. $f = 0$ and $f = 0.2$. Young's modulus for the insulating layer is $E_{\text{ins}} = 5\text{GPa}$. The effective strain is calculated according to equation (2.4) and the values are extracted as described in chapter 2.3.4.

Figures 3.26 and 3.27 give the residual effective stresses ϵ_{eff} after each rollover of pure rolling i.e. $f=0$.

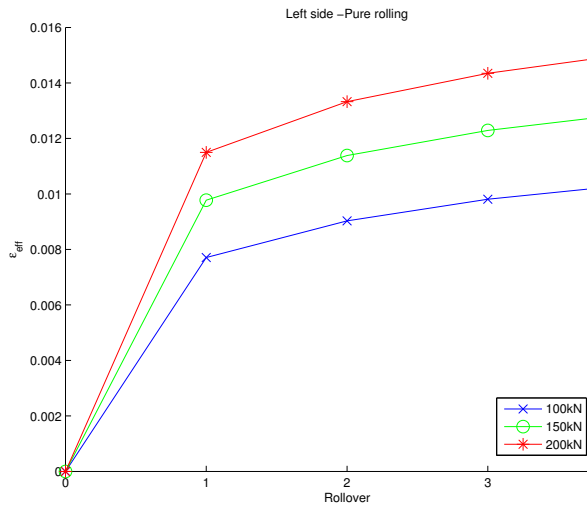


Figure 3.26: Influence of vertical load magnitude on the residual ϵ_{eff} . Left hand side, pure rolling

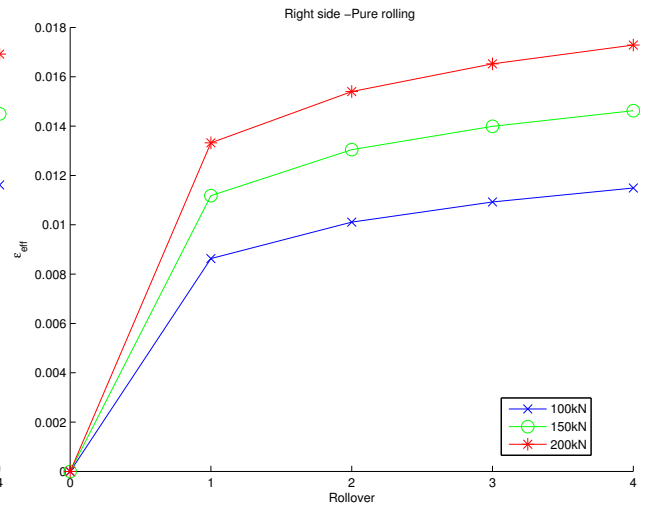


Figure 3.27: Influence of vertical load magnitude on the residual ϵ_{eff} . Right hand side, pure rolling

As expected the effective strain ϵ_{eff} increases with an increased load. By increasing the vertical load F_y from 100 kN to 200 kN the value of the residual ϵ_{eff} after the 4th rollover increases by 45% on the left hand side and by 50% on the right hand side. Also the residual ϵ_{eff} is higher on the right hand side than on the left hand side. For the built-in Abaqus material model the equivalent plastic strain ϵ_p was higher on the left hand side for the same load and the same stiffness of the insulating layer. The difference between the right and the left hand sides is not significant so the difference between the two material models can probably be explained partly by the different constitutive relations, and partly by the fact that the residual effective strain ϵ_{eff} and the plastic strain ϵ_p are not directly comparable.

Now consider cases when a moment is applied, i.e. $f = 0.2$

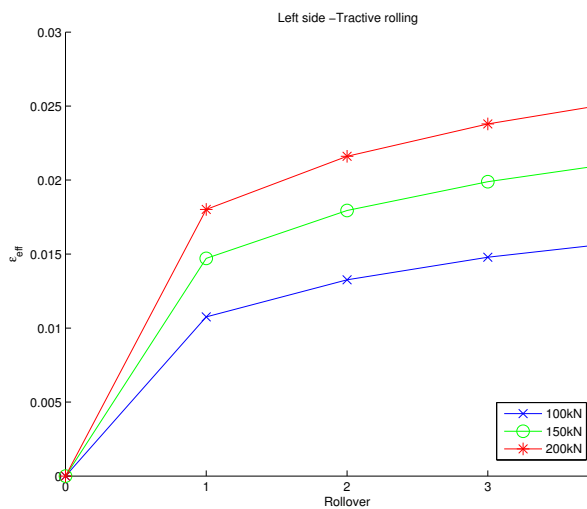


Figure 3.28: Influence of vertical load magnitude on the residual ϵ_{eff} . Left hand side, tractive rolling, $f = 0.2$.

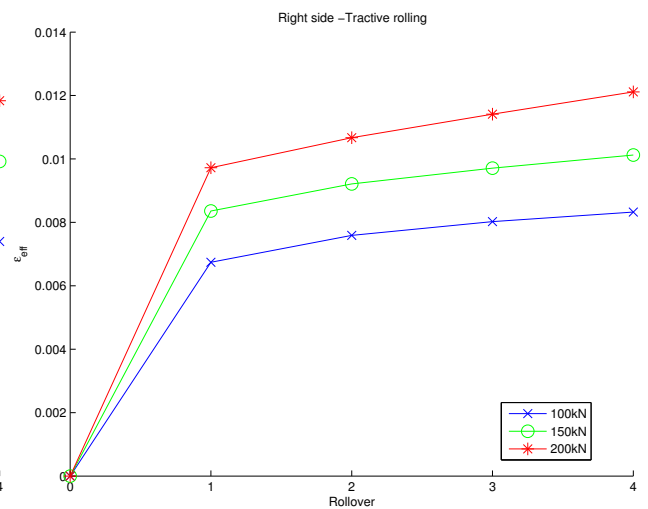


Figure 3.29: Influence of vertical load magnitude on the residual ϵ_{eff} . Right hand side, tractive rolling, $f = 0.2$.

In figures 3.28 it is seen that the residual effective strain ϵ_{eff} is much higher on the left hand side with the applied traction, about 70% increase for $F_y = 200$ kN after the 4th rollover. For the right hand side the residual ϵ_{eff} decreases. This behavior is the same as for the built in Abaqus-material model. A possible reason is given in the following section.

3.4.2 Traction vs. pure rolling

It is interesting to evaluate the stress–strain curves for the steel on both sides with and without the applied traction i.e. with $f = 0$ and $f = 0.2$. The applied vertical force is $F_y = 150$ kN and the stiffness of the insulating layer is $E_{\text{ins}} = 5$ GPa . The material model of the steel is the Custom constitutive model. The values are evaluated at a distance and depth of 1.5 mm from the insulating layer at both sides as described in chapter 2.3.4. The element mesh seed size is 0.5 mm in the insulating layer and the surrounding steel.

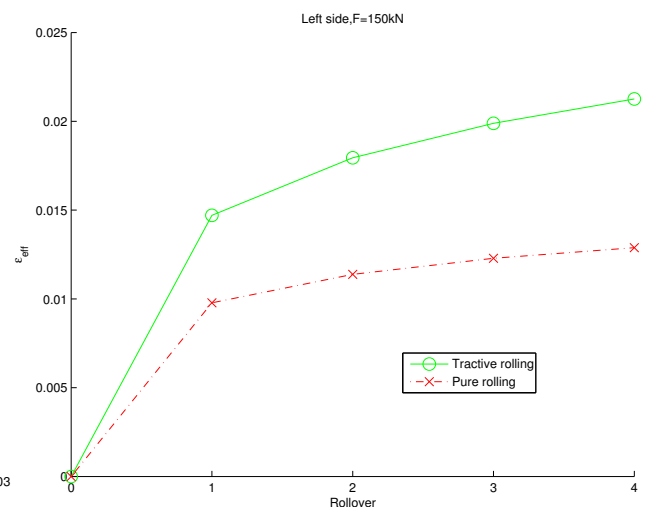
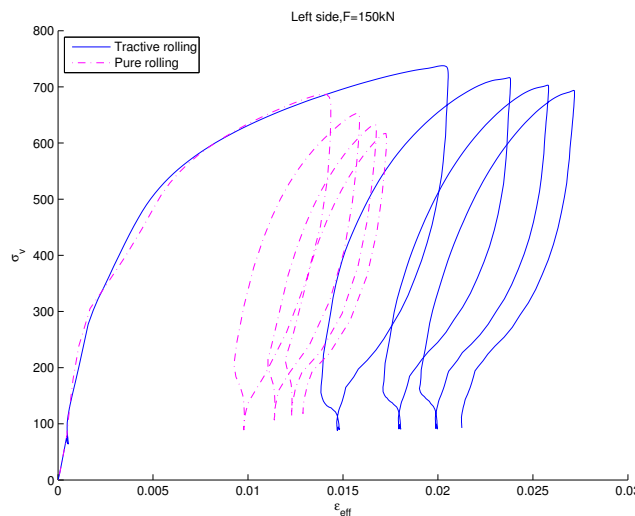


Figure 3.30: Stress strain curve – Pure rolling and tractive rolling. Figure 3.31: Residual effective strain ϵ_{eff} at the end of each cycle.

Figures 3.30 and 3.31 show the stress–strain curves and the residual effective strain ϵ_{eff} for the left hand side of the insulating layer. For tractive rolling the steel yields much more than for pure rolling.

In figures 3.32 - 3.33 the same corresponding stress–strain curves on the right side of insulating layer are plotted. Here the steel yields more when there is no applied moment. The reason for this is the yield criteria of the material. A very simplified diagram can be seen in figure 3.34.

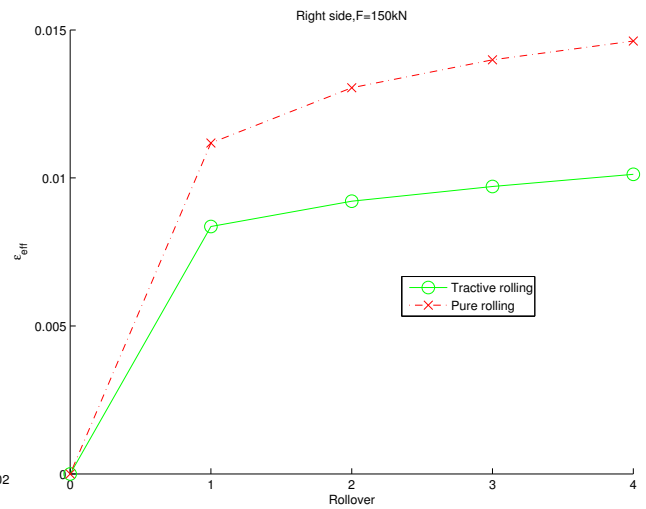
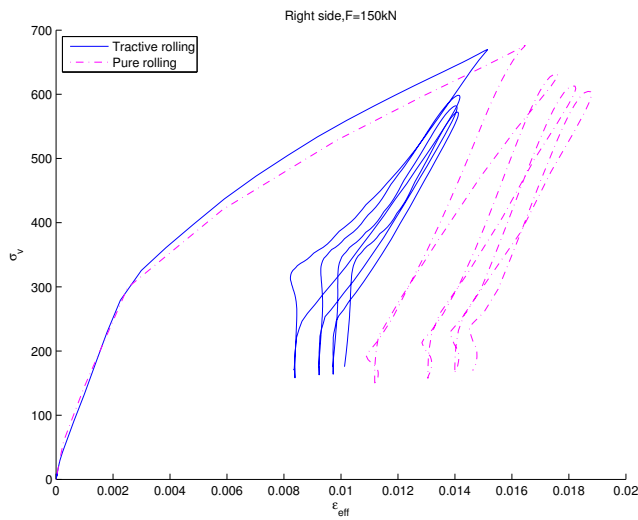


Figure 3.32: Stress–strain curve–Tractive vs. pure rolling. Figure 3.33: Residual effective strain ϵ_{eff} at the end of each cycle.

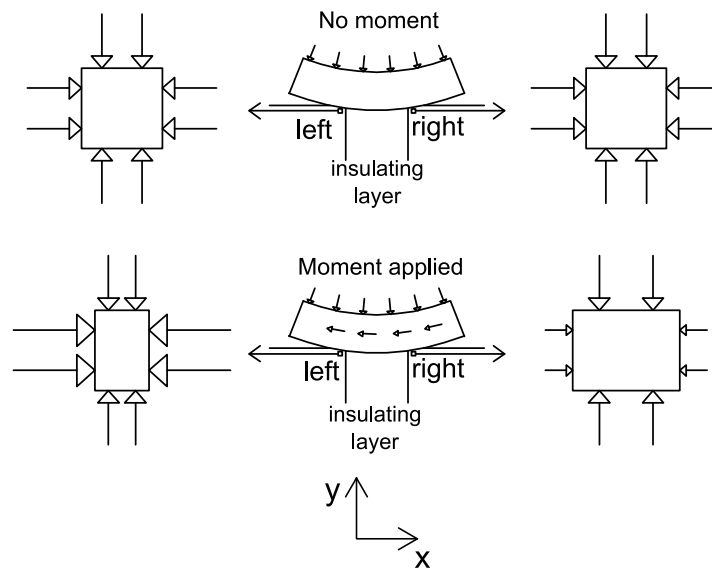


Figure 3.34: Simplified diagram showing the stressing of a material element in the steel on both sides of the insulating layer. The quivers indicate the magnitude of σ in different directions.

When there is no moment applied ($f = 0$) the main stress in the material on both sides is compressive σ_{yy} due to the weight of the train and also compressive σ_{xx} when the wheel sinks into the insulating layer. With the moment applied on the wheel center the compressive σ_{xx} on the left hand side of the insulating layer increases which causes the material to "lift" due to the Poisson effect i.e. when compressed in one direction it expands in the other directions. This causes a higher contact stress on the left side and the material yields more. However on the right side the material is stretched out along the x -axis towards the insulating layer which causes a lower compressive σ_{xx} , that reduces the yielding. This also explains better why increasing the stiffness of the insulating layer causes more yielding on the right hand side for a tractive rolling, the steel can not stretch as much in the negative x -directions when the insulating material gets stiffer.

3.4.3 Variable Young's modulus of the insulating layer

These simulations were conducted in the same manner as for the built-in Abaqus model for the steel material. The vertical load was $F_y = 150$ kN on the wheel center and the simulations were conducted with and without traction i.e $f = 0$ and $f = 0.2$. ϵ_{eff} plotted here in the following graphs is the residual ϵ_{eff} after each rollover and is calculated according to equation (2.4).

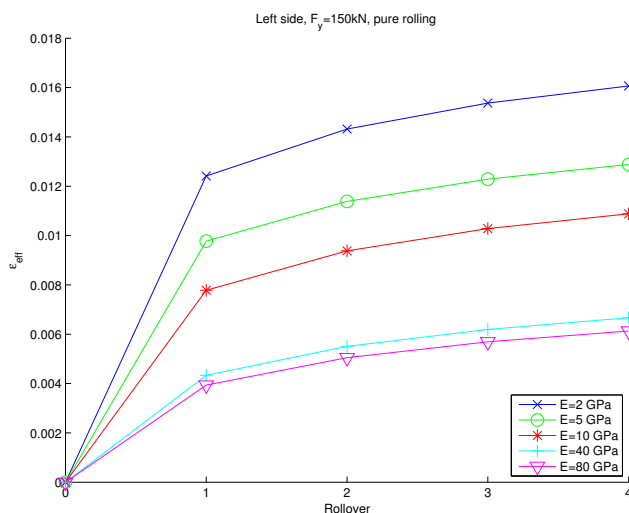


Figure 3.35: Variable Young's modulus, left hand side, pure rolling.

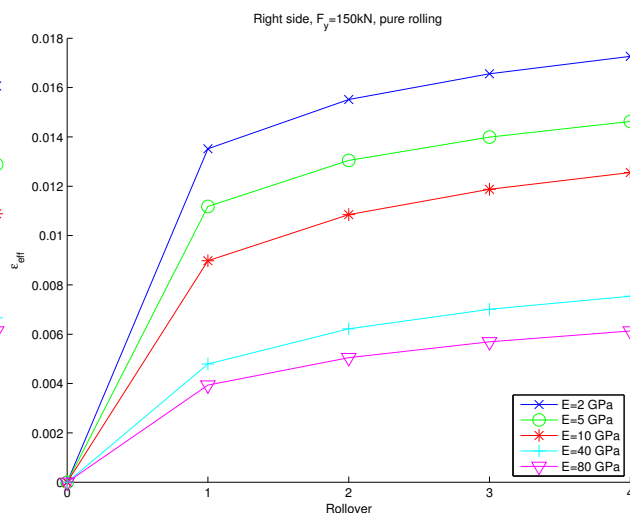


Figure 3.36: Variable Young modulus, right hand side, pure rolling.

From figures 3.35–3.36 it is clear that it is beneficial for the steel to have a stiffer insulating layer. The results are similar to those featuring the built-in ABAQUS model, although there is it much larger difference between residual ϵ_{eff} and ϵ_p when E_{ins} changes from 2 GPa to 10 GPa. Since the custom model is designed for large strains but the Abaqus model not, these results are more valid since the strains are large in the steel around the insulating layer.

Figures 3.37 and 3.38 show the influence of the insulating stiffness when the moment M is applied i.e. $f = 0.2$. The steel yields less on the left side with an increased stiffness of the insulating layer. For the same load in the built-in Abaqus model there was so little difference between ϵ_p after the 4th rollover that there was no noticeable gain of increasing the stiffness of the insulating layer. On the right hand side the yielding decreases for increasing stiffness up to $E_{\text{ins}} = 10$ GPa then the yielding increases again. When running this same test for the Abaqus built-in model, the yielding increased for all increasing E_{ins} on the right hand side.

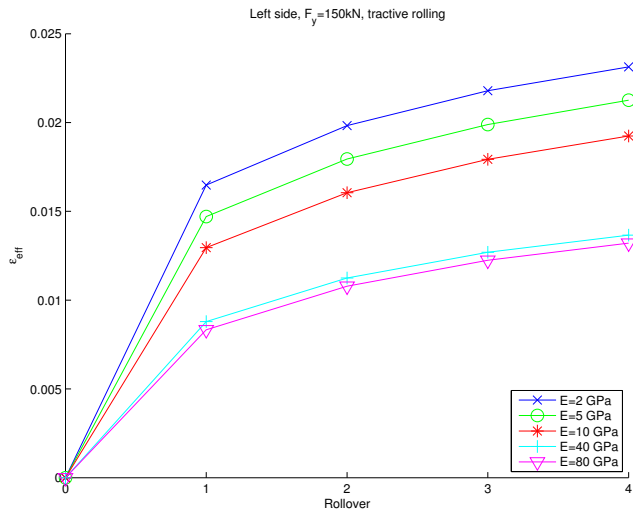


Figure 3.37: Variable Young modulus, left side. Tractive rolling

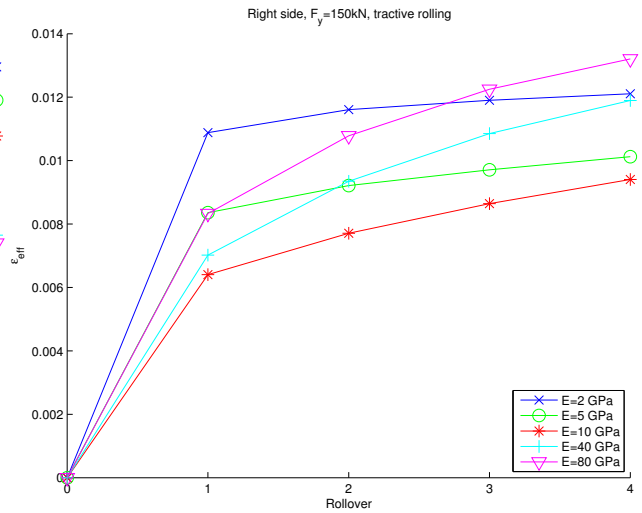


Figure 3.38: Variable Young modulus, right side. Tractive rolling

3.4.4 Many rollovers–Stabilization

To see if the stress-strain curve will stabilize and investigate if the values of ϵ_{eff} would converge, one simulation with 16 rollovers was performed. This simulation would also test the decision to simulate only 4 rollovers in the previous simulations. The vertical load is $F_y = 150 \text{ kN}$ and the simulations featured tractive rolling ($f = 0.2$). The Young's modulus of the insulating layer was $E_{\text{ins}} = 5 \text{ GPa}$.

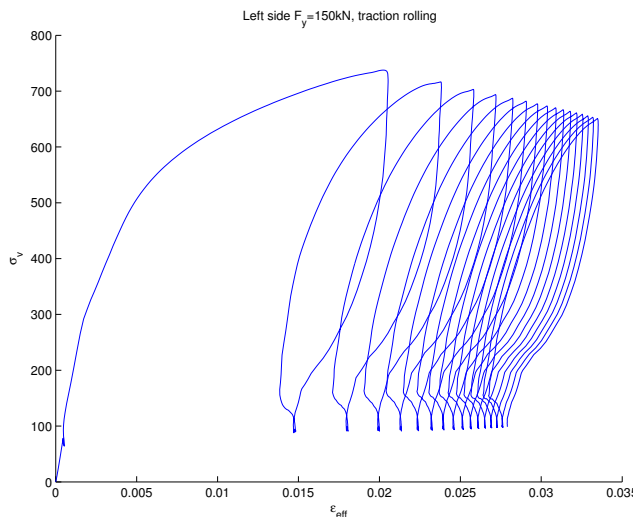


Figure 3.39: σ_v vs. ϵ_{eff} , left hand side, 16 rollovers

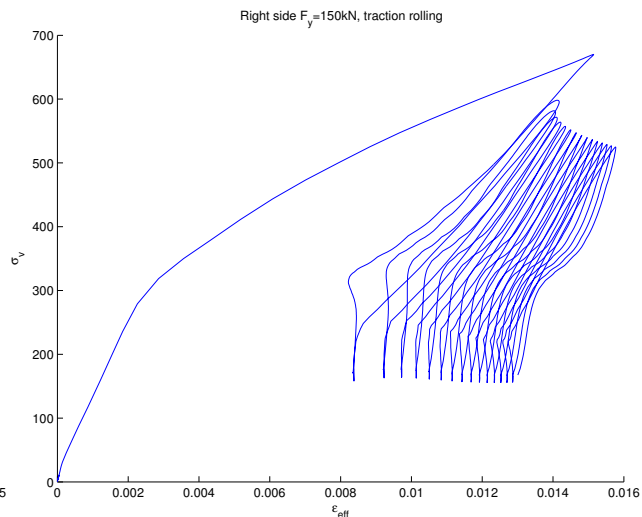


Figure 3.40: σ_v vs. ϵ_{eff} , right hand side, 16 rollovers

Figures 3.39 and 3.40 show that the stress–strain relations for both sides are far from stabilizing. It can further be seen that the strain accumulation decreases between wheel passages. By looking at the two figures it can be seen that most of the yielding happens in the first 3–6 rollovers so it looks as if taking 4 rollovers is a good balance between accuracy and simulation time since the trend of the curves can easily be seen only by looking at 4 rollovers.

3.5 Limitations of using static analysis

The wheel mass was assumed to be $m_{\text{wheel}} = 750$ kg and the vertical load $F_y = 150$ kN with pure rolling i.e. $f = 0$. The insulating layer stiffness is $E_{\text{ins}} = 5$ GPa in the Abaqus simulation. The wheel displacement from Abaqus are from the 4th and final rollover and the material model for the railway steel is the custom model as described in chapter 2.2.4.

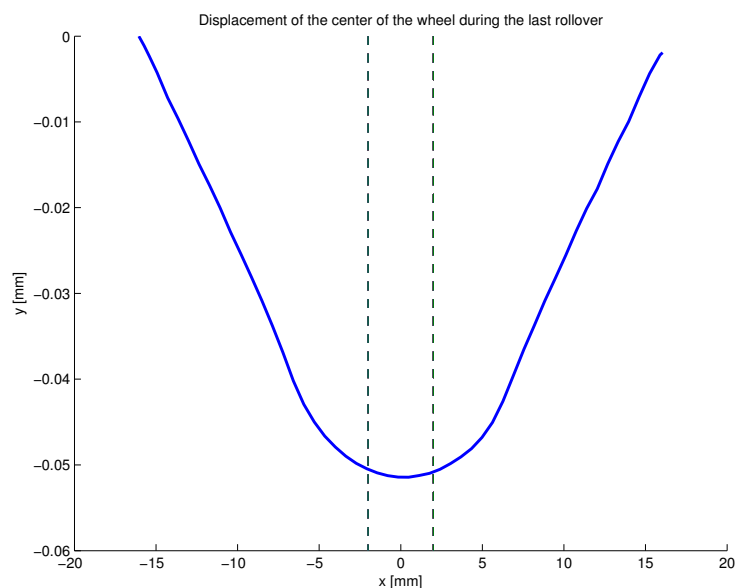


Figure 3.41: Wheel displacement during the last rollover (4th). The dotted lines show where the insulating layer is. Note that the scales on the axes are not equal.

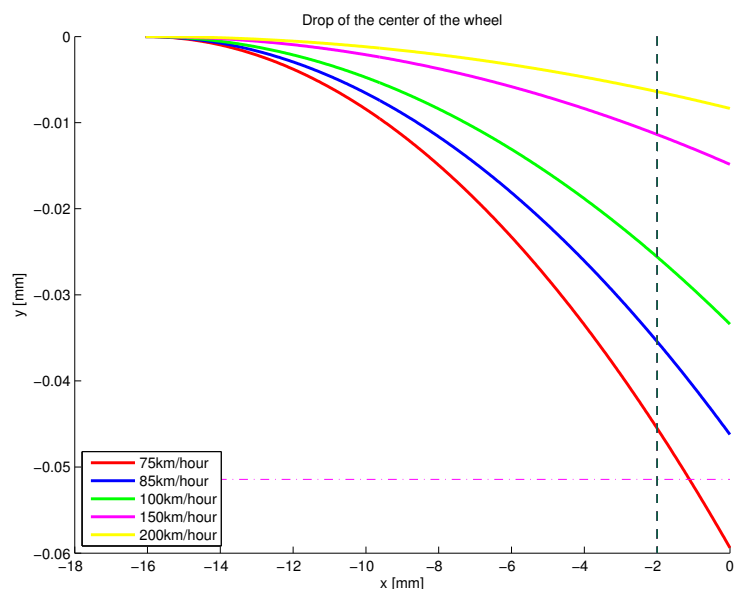


Figure 3.42: Wheel displacement due to the free-falling of the wheel. The dotted line represents where insulating layer starts, the horizontal dashed-dotted line represents the maximum vertical displacement from the quasi-static Abaqus-simulation.

It is seen in figures 3.41 and 3.42 that even if the wheel is allowed to fall freely due to the weight of the train and we assume there is no reaction force from the rail it can not fall the vertical distance corresponding to the evaluated displacement when traveling with a speed more than roughly 85km/h. Just by these simple calculations it is clear

that the results from dynamic simulations would not be the same. Further in the static simulation the vertical force on the rail surface from the wheel is constant in each rollover, in a dynamic simulation however this force would decrease when entering the insulating layer and the wheel would accelerate downwards, then the force would increase again when the wheel impacts the far rail end post. The results from a dynamic simulation would therefore cause less yielding on the left side and more on the right side as compared to the static simulation (wheel traveling from left to right as before).

4 Discussion

Hyper-elastic insulating material: When comparing hyper-elastic insulating material to linear-elastic material the difference in stresses and displacements were almost non-existent for a wide range of Young's moduli in the insulating material E_{ins} 2–80 GPa. The displacements in the insulating material are just not large enough for the hyper-elastic material model to behave non-linear so there is no need to use a hyper-elastic constitutive model for an insulating gap that is only 4 mm.

Increasing stiffness of the insulating material: Increasing the stiffness of the insulating layer decreases the yielding in steel on both sides under pure rolling conditions. The standard Abaqus constitutive model for the rail material did not give quite clear results regarding if it was better for the tractive rolling. However the Custom model indicated that this was the case when increasing from 2 GPa to 10 GPa. The results from the Custom model should be more accurate since the Custom model is especially designed for railway steels with large strains. Note though that the material parameters for both models are evaluated using test data from real rail steels in [6] and [5]. When increasing the stiffness, the shear stress σ_{xy} between the interface of the two materials increases, thus it is necessary to optimize the value of the Young's modulus with respect to the strength of the glue that ties the materials together.

Inclined joint: The results from having an inclined joint (defined by the inclination angle θ) show that the contact pressure between the wheel surface and the track surface increases which causes an increased yielding in the steel. Regarding the shear stresses between the two materials (values extracted from the integration points closest to the steel from the insulating layer) $\sigma_{x'y'}$ decreases while $\sigma_{y'z'}$ increases consequently it was not beneficial for the glue between the two materials to have an inclined joint either.

Influence of load magnitude: With increased vertical loading of the wheel the strain magnitudes in the steel increases as expected.

When comparing the effect on the steel with and without traction the straining increased significantly on the left hand side (train traveling from left to right and moment applied clockwise). However the strain magnitudes decreased on the right side.

Dynamic simulation vs. quasi-static simulation: By using simple Newtonian dynamic equations and comparing the displacement of the wheel from the static simulation it was shown that it is not quite valid to use quasi-static simulations when the train is traveling more than around 85km/h when the applied load is $F_y=150$ kN. The time that it takes the wheel to travel over the insulating layer is so small that it can not deflect the same distance (y -direction) as in the static simulation. Consequently, predictions from dynamic simulations would differ. However the resulting computational demand in running

full dynamic simulations are currently not realistic. More about dynamic simulations for insulating joints can be found in [2].

5 Acknowledgments

Special thanks to Johan Sandström for all the help and support he gave me during during the preparation of this essay. I also want to thank Magnus Ekh for all the help he gave me.

A Material parameters

A.1 Built in Abaqus constitutive model

$$E = 200 \text{ GPa} \quad \nu = 0.3 \quad \sigma_0 = Y = 443 \text{ MPa} \\ C = 66 \text{ GPa} \quad \gamma = 636$$

where E is the Young's modulus, ν Poisson's ratio, $\sigma_0 = Y$ the yield limit and C and γ are the kinematic hardening parameters. The values are evaluated using experimental data for rail steel R260 (UIC900A) see [5]

A.2 Custom model

The values of the input parameters are evaluated using experimental data for railway steel 900A (R260).

$$E = 199 \text{ GPa} \quad \nu = 0.293 \quad Y = 295 \text{ MPa} \\ \beta = 0.3 \quad H_1 = 34 \text{ GPa} \quad H_2 = 4.4 \text{ GPa} \\ H_3 = 0.73 \text{ GPa} \quad H_4 = 0.408 \text{ GPa} \quad Y_1 = 0.250 \text{ GPa} \\ Y_2 = 2 \text{ GPa} \quad Y_3 = 10 \text{ GPa} \quad Y_4 = 34 \text{ GPa}$$

E is the Young's modulus of the material, ν is the Poisson's ratio, Y is the initial yield limit, H_i are the hardening moduli, Y_i saturation stresses. β governs the combination of Armstrong–Frederick and Burlet–Cailletaud hardening. The values are derived in [6]

References

- [1] Norman E. Dowling. *Mechanical behavior of materials*. Pearson Prentice Hall, 2007.
- [2] J.C.O Nielsen E. Kabo and A. Ekberg. Prediction of dynamic train-track interaction and subsequent material deterioration in the presence of insulated rail joints. 2006.
- [3] Gerhard A. Holzapfel. *Nonlinear Solid Mechanics*. Wiley, 2006.
- [4] Richard D. Wood Javier Bonet. *Nonlinear Continuum Mechanics for Finite Element Analysis*. Cambridge, 2008.
- [5] Goran Johansson. *On the modeling of large ratcheting strains and anisotropy in pearlitic steel*. PhD thesis, Chalmers University of Technology, Department of Applied Mechanics, SE 412 96 Göteborg, Sweden, 2006.
- [6] Göran Johansson. Abaqus-umat implementation of large strain hyperelasto-plastic model with kinematic hardening. October 2007.
- [7] Johan Sandström and Johan Anders Ekberg. Numerical study of the mechanical deterioration of insulated rail joints. *Proc Inst Mech Eng Part F J Rail and Rapid Transit*, 223:265–273, 2009.